Accepted by ApJ 2015 November
Preprint typeset using LaTeX style emulateapj v. 5/2/11

arXiv:1511.05528v1 [astro-ph.EP] 17 Nov 2015

CHARACTERIZING TRANSITING EXOPLANET ATMOSPHERES WITH JWST

Thomas P. Greene[1]
NASA Ames Research Center, Space Science and Astrobiology Division, M.S. 245-6; Moffett Field, CA 94035

Michael R. Line[2,3,4,5], Cezar Montero, and Jonathan J. Fortney
Department of Astronomy and Astrophysics, University of California, Santa Cruz, CA 95064

Jacob Lustig-Yeager
Department of Astronomy, Box 351580, University of Washington, Seattle, WA 98195

Kyle Luther
Department of Physics, University of California, 366 LeConte Hall MC 7300, Berkeley, CA 94720
Accepted by ApJ 2015 November

ABSTRACT

We explore how well James Webb Space Telescope (JWST) spectra will likely constrain bulk atmospheric properties of transiting exoplanets. We start by modeling the atmospheres of archetypal hot Jupiter, warm Neptune, warm sub-Neptune, and cool super-Earth planets with clear, cloudy, or high mean molecular weight atmospheres. Next we simulate the $\lambda = 1 - 11$ μm transmission and emission spectra of these systems for several JWST instrument modes for single transit and eclipse events. We then perform retrievals to determine how well temperatures and molecular mixing ratios (CH_4, CO, CO_2, H_2O, NH_3) can be constrained. We find that $\lambda = 1 - 2.5$ μm transmission spectra will often constrain the major molecular constituents of clear solar composition atmospheres well. Cloudy or high mean molecular weight atmospheres will often require full $1 - 11$ μm spectra for good constraints, and emission data may be more useful in cases of sufficiently high F_p and high F_p/F_*. Strong temperature inversions in the solar composition hot Jupiter atmosphere should be detectable with $1 - 2.5+$ μm emission spectra, and $1 - 5+$ μm emission spectra will constrain the temperature-pressure profiles of warm planets. Transmission spectra over $1 - 5+$ μm will constrain [Fe/H] values to better than 0.5 dex for the clear atmospheres of the hot and warm planets studied. Carbon-to-oxygen ratios can be constrained to better than a factor of 2 in some systems. We expect that these results will provide useful predictions of the scientific value of single event JWST spectra until its on-orbit performance is known.

Subject headings: methods: statistical — planets and satellites: atmospheres — planets and satellites: composition — techniques: spectroscopic

1. INTRODUCTION

There are now well over a thousand confirmed exoplanets, ranging from hot to cold and large to small worlds. Characterizing the atmospheres of a diversity of planets is critical to understanding their bulk compositions, formation (and any migration), energy balance, and atmospheric processes (e.g., see Crossfield 2015; Madhusudhan et al. 2014; Burrows & Orton 2010; Heng & Showman 2015; Seager & Deming 2010; Burrows 2014).

Much of the atmospheric characterization work has come from the acquisition and interpretation of transmission and emission spectroscopy of transiting planets by the Hubble and Spitzer space telescopes. The transmission or emission spectra of Hot Jupiters (e.g., HD 189733b, WASP-43b), warm Neptunes (e.g., GJ 436b, HAT-P-11b), and warm sub-Neptunes (e.g., GJ 1214b) are all being studied extensively with HST, Spitzer, and other facilities. The near-IR spectra of cool or warm super-Earths like K2-3b/c/d will soon be observed with HST, and they will likely be prime candidates for JWST spectroscopy. Observations to date have produced a variety of important discoveries such as the detection of H_2O absorption, now clearly seen in a variety of planets using a variety of instruments. HST NICMOS and HST WFC3 G141 find strong water absorption in about a dozen hot Jupiters (e.g., Kreidberg et al. 2014b, 2015; Deming et al. 2013; Crouzet et al. 2012; Swain et al. 2009) and a warm Neptune-sized planet (Fraine et al. 2014). Atmospheric retrieval techniques have been applied to the data in order to determine the abundances (or upper limits) of molecules such CO, CO_2, and CH_4 in addition to H_2O in $\sim$ 10 exoplanet atmospheres (e.g., Madhusudhan & Seager 2009; Madhusudhan et al. 2011; Lee et al. 2012; Line et al. 2012; Barstow et al. 2013a,b; Benneke & Seager 2012, 2013; Line et al. 2013a, 2014a; Benneke 2015; Waldmann et al. 2015). Molecular abundance determinations have been used to constrain atmospheric C/O ratios (e.g., Benneke 2015; Line et al. 2014a; Madhusudhan

[1] Correspondence to be directed to tom.greene@nasa.gov
[2] Hubble Postdoctoral Fellow
[3] NASA Ames Research Center, Moffett Field, CA
[4] Bay Area Environmental Research Institute, Petaluma, CA
[5] School of Earth and Space Exploration, Arizona State University, Tempe, AZ

et al. 2011) which can potentially help diagnose where a planet formed relative to the H_2O and CO ice lines in its protoplanetary disk (Öberg et al. 2011). Atmospheric metallicity determinations relative to the host star have also been used to infer formation possibly via a core accretion (e.g., Kreidberg et al. 2014b). Temperature inversions have been suggested to explain the emission spectra of a number of hot Jupiters (e.g., see Fortney et al. 2008; Knutson et al. 2010, and references therein), indicating the presence of visible or UV stratospheric absorbers. However, recent work by Line et al. (2014a) indicates no strong statistical evidence for inversions in a sample of 9 observed planets, but the very hot Jupiters HAT-P-7b (Christiansen et al. 2010) and WASP-33b (Haynes et al. 2015) do appear to have temperature inversions at the present time (see also Crossfield 2015). Determining the frequency of inversions over a variety of bulk planetary properties is important for understanding chemical processes (e.g., impact of C/O on high altitude absorbers) and the overall energy balance in these planets' atmospheres.

Despite these advances, there are still considerable uncertainties in the compositions, temperatures, and origins of exoplanet atmospheres. Numerous early HST and Spitzer detections of molecular features and temperature inversions have been called into question or disproven with subsequent higher precision observations, more sophisticated data analysis, and powerful modern retrieval techniques for molecular abundances and temperature-pressure (hereafter T-P) profiles (e.g., Benneke 2015; Schwarz et al. 2015; Line et al. 2014a; Diamond-Lowe et al. 2014; Gibson et al. 2011). Clearly, we need to better determine the compositions of exoplanet atmospheres, what planets have stratospheric temperature inversions under what conditions, how closely planet elemental abundances match their host stars, and where planets formed in their disks. Addressing or resolving these specific questions would significantly advance our understanding of exoplanet atmospheres:

> Do any highly insolated planets have hot stratospheres, and what absorbers are causing these temperature inversions if they exist?
>
> What are the nature of super-Earth (1.5 – 2 $R_\oplus$) planet atmospheres; are they mostly H and He or are they dominated by high mean molecular weight species like Earth and Venus?
>
> How do clouds inhibit our ability to infer molecular abundances?
>
> What are the C-to-O ratios in planetary atmospheres, how does this compare to their host stars, and what does this imply about where planets formed in protoplanetary disks?
>
> How to the metal abundances of planets compare to their host stars, and does this vary by planet mass as it does for giants in our solar system?
>
> How far from chemical equilibrium can exoplanet atmospheres be driven, and what causes this??

High quality JWST observations may characterize transiting exoplanet atmospheres well enough to address these questions significantly in the near future (launch is currently scheduled for 2018 October). JWST's large aperture (6.5-m), numerous spectroscopic modes over $\lambda = 0.6-28$ μm, good thermal stability, and applications of lessons learned from other observatories will ensure that it collects the highest quality exoplanet transmission and emission spectra. Numerous studies are providing assessments of how well JWST is expected to characterize exoplanet atmospheres. Beichman et al. (2014) present many details of JWST's instruments and recommend appropriate modes for observing transiting exoplanets. Cowan et al. (2015) report that JWST is expected to characterize dozens of giant planets over its mission lifetime, but observations of cool, small planet ("temperate terrestrial") atmospheres may require ∼100 days each. Batalha et al. (2015) find that JWST NIRSpec should be able to measure the $\lambda = 1-5$ μm transmission spectra of nearby (3 – 50 pc), cool ($400-1000$ K), low-mass ($1-10M_\oplus$) planets orbiting mid-M dwarfs with moderate signal-to-noise ratios (SNRs) after summing 25 transits. Barstow et al. (2015) performed JWST data simulations and atmospheric retrievals to investigate the impacts of starspots and other systematic errors that shift different spectral wavelength ranges that are not obtained simultaneously.

These studies have greatly improved our understanding of the promises and potential limits of JWST data. However, we still do not understand how well JWST will be able to quantitatively characterize different types of planets in the above ways. We also need to understand better what observing modes will be most useful for addressing specific questions. This is an important assessment because most transiting planets with bright host stars ($J \lesssim 11$ mag) will need to be observed 4 separate times to collect their entire $\lambda = 0.7-12+$ μm spectra (e.g., see Beichman et al. 2014), and JWST time will be extremely precious. We perform and discuss such quantitative assessments in this contribution.

We investigate how well temperature and molecular volume mixing ratio constraints from JWST observations can address these big picture questions by analyzing simulated observations of a diverse range of planet types. We start by presenting a diverse set of planetary systems that span what we think are the typical planet types in §2. We describe the atmospheric models and the retrieval technique in §3. Next we describe the instrument signal and noise models we use to create simulated JWST spectra in §4. The retrieval results including the molecular and temperature constraints are presented in §5. We apply these results to assess planet carbon-to-oxygen ratios, metallicities, and probes of disequilibribum chemistry in §6 and the big picture questions these can address. Finally, we summarize our conclusions in §7.

2. SIMULATED PLANETS

We assemble a set of 4 fiducial planetary systems to assess how well JWST will be able to characterize exoplanet atmospheres in the early years of its mission. These planets range from hot ($T_{\rm eq}$ = 1500 K) to cool ($T_{\rm eq}$ = 500 K) and large (1.36 $R_{\rm J}$) to small (0.19 $R_{\rm J}$). This combination of sizes and temperatures maps well onto the now established planet archetypes of hot Jupiters, warm Neptunes, warm sub-Neptunes, and cool super-Earths. We select the physical parameters of a

well known system from each of these categories to assemble our set of 4 systems to model. We model their atmospheres as either clear with solar elemental abundances, cloudy with solar elemental abundances, and for the smaller planets clear with enhanced elemental abundances so as to result in high mean molecular weight (HMMW) atmospheres.

Constant-with-altitude molecular abundances were generated assuming broad consistency with thermochemical equilibrium given the effective temperature of the planet and the elemental abundances (computed with the Chemical Equilibrium with Applications code (Gordon & McBride 1994; Visscher & Moses 2011; Line et al. 2010; Moses et al. 2011)[6], and the HMMW atmospheres were either 1000× solar metallicity or pure H_2O. The 1000× solar compositions correspond to mean molecular weight μ=15 for the warm Neptune and μ = 16.8 for the warm sub-Neptune atmospheres (see Fortney et al. (2013)). It is not clear whether 1000× solar metallicity is possible since accreted planetesimals include hydrogen if they are icy (Fortney et al. 2013), preventing this level of atmospheric metallicity. Nevertheless, we believe that this is a useful bounding case. The 100% H_2O cool super-Earth atmosphere has a molecular weight of μ = 18 and corresponds to an [Fe/H] = 2.77 (588× solar metallicity)[7]. The set of planet types, system parameters, and atmospheric molecular mixing ratios are given in Tables 1, 2, and 3. Actual small, cool planets may not be in chemical equilibrium, and we discuss how well we can detect disequilibrium chemistry in §6.3.

3. MODELING AND RETRIEVAL APPROACH

The emission spectra are computed using the forward model described in Line et al. (2013a) and subsequent upgrades described in Diamond-Lowe et al. (2014) and Stevenson et al. (2014). The transmission spectra are computed with the forward model described in Line et al. (2013b), Swain et al. (2014), and Kreidberg et al. (2014b). We then use a derivative of the CHIMERA[8] retrieval suite (Line et al. 2013a,b) to determine the degree of constraints on temperatures and abundances from simulated observations of the transmission and emission spectra (see §4). The molecular opacities described in §2.3 of Line et al. (2015) were used for computing all forward and retrieval model spectra.

While atmospheres are undoubtably complicated, we choose a relatively simple 1-D parameterization. Since we are using the same forward model to generate the synthetic spectra as the retrieval, this should not be a problem for assessing the impact of JWST data quality. This will allow us to strictly explore the role that the JWST instrumental noise properties and spectral coverage have on setting the atmospheric constraints. We perform a preliminary exploration of retrieval assumptions and priors and their inherent biases on the retrieved results later in this work (see §5.1), and a more thorough analysis will be the subject of a forthcoming paper.

Because of the different viewing geometries, the atmospheres used in transmission are parameterized differently than the atmospheres used to generate the emission spectra. However, both use the same set of uniform-with-altitude molecular abundances. These include H_2O, CH_4, CO, CO_2, NH_3, and N_2 (except in emission as it has no consequence on the emission spectra). Any remaining gas is assumed to be a mixture of solar composition H_2/He. N_2 is the dominant nitrogen bearing species at high temperatures, but it has no spectroscopic features unless in high concentrations (Schwieterman et al. 2015). We include it here as a trace gas simply to contribute to the mean molecular weight of atmospheres in transmission spectra. The fiducial abundances are again chosen to be broadly consistent with thermochemical equilibrium at the given scale height temperature. For all but the hot-Jupiter scenario we deplete 2-oxygen atoms per every magnesium to emulate oxygen loss due to enstatite (Mg_2SiO_4) condensation. The impact of various absorption features for each of these species in the clear solar composition hot Jupiter and warm Neptune transmission and emission model spectra in Figure 1.

The transmission spectra are generated with 11 free parameters, 6 of which are the volume mixing ratios of the molecular gasses noted above. The remaining 5 parameters are as follows: First, an effective scale height temperature (T). This will directly impact the amplitude of the spectral features. For simplicity, we assume isothermal atmospheres for the transmission spectra at the approximate equilibrium temperature (without truly knowing the albedo or redistribution) of the planet in question. Barstow et al. (2013a, 2015) demonstrated that there may be potential biases in real atmospheres if isothermal atmospheres are assumed, but that it will be incredibly difficult to actually retrieve detailed temperature *profile* information from transmission spectra. Second, we use a scaling to the fiducial 10 bar planet radius (xR_p). This parameter manifests itself as a DC offset in the spectra as well as a minor impact on the amplitude of the features. Third, we include an opaque gray cloud parameterized with a cloud-top pressure (P_c) which we set to 1 mbar. The atmospheric transmittance at atmospheric levels deeper than the cloud top is set to zero. Several measured flat exoplanet transmission spectra have been reasonably well described with such a parameterization (Line et al. 2013b; Kreidberg et al. 2014a; Knutson et al. 2014). We also model hazes in an ad-hoc fashion using the following approximation (e.g., Lecavelier Des Etangs et al. 2008):

$$\sigma = \sigma_0 (\frac{\lambda}{\lambda_0})^{-\beta}. \quad (1)$$

σ_0 is the magnitude of the haze cross-section relative to H_2 Rayleigh scattering at 0.4 μm, and β is the wavelength power law index that describes the slope. While the $\lambda \geq 1$ μm wavelength range explored in this study will not provide constraints on these parameters, we in-

[6] We note that thermochemical equilibrium generally does not produce constant-with-altitude mixing ratio profiles. However, for the dominant carbon-bearing species and H_2O, constant with altitude generally does occur in equilibrium. For the less dominant species we choose a representative value along a non-uniform vertical profile.

[7] It is impossible to generate a pure H_2O atmosphere thermochemically by scaling the solar elemental abundances. The metallicity value here is determined by taking 0.5 (the ratio of metals, O, to hydrogen (2H)) and dividing that by the solar metal fraction value of 8.5×10^{-4}

[8] Instead of using the Differential Evolution Markov chain Monte Carlo as in Line et al. (2013b, 2014a), we use the EMCEE routine of Foreman-Mackey et al. (2014)

Table 1
Planetary Systems Modeled

Planet Type	System Parameters	Composition	Clouds	Geometry
Hot Jupiter	HD 209458b	1× Solar	Clear	Trans, Emis
			1 mbar	Trans
Warm Neptune	GJ 436b	1× Solar	Clear	Trans, Emis
			1 mbar	Trans
		1000× Solar	Clear	Trans, Emis
Warm Sub-Neptune	GJ 1214b	1× Solar	Clear	Trans, Emis
			1 mbar	Trans
		1000× Solar	Clear	Trans, Emis
Cool Super-Earth	K2-3b	1× Solar	Clear	Trans, Emis
			1 mbar	Trans
		100% H_2O	Clear	Trans, Emis

Table 2
Fiducial Planetary System Parameters

Planet Type	System Parameters	T_* (K)	R_* ($R_\odot$)	K (mag)	$T_{\rm eq}$[a] (K)	$M_{\rm p}$ ($M_\oplus$)	$R_{\rm p}$ ($R_\oplus$)	H[b] (km)	T_{14} (s)
Hot Jupiter	HD 209458b	6065	1.155	6.3	1500	220	15	560	11,000
Warm Neptune	GJ 436b	3350	0.464	6.1	700	23	4.2	190	2740
Warm Sub-Neptune	GJ 1214b	3030	0.211	8.8	600	6.5	2.7	230	3160
Cool Super-Earth	K2-3b	3900	0.561	8.6	500	5.3[c]	2.1	150[c]	9190

Note. — Tabulated system values were taken from the exoplanets.org compilation (Han et al. 2014) and Crossfield et al. (2015).

[a] Equilibrium temperature $T_{\rm eq}$ was computed from the listed system values assuming albedo = 0 and energy re-distribution over 4π str.

[b] The planetary atmosphere scale height $H = kT_{\rm eq}/(\mu m_H g)$ for the clear solar atmosphere of each planet ($\mu = 2.3$) is provided as a convenience for scaling to other systems.

[c] The mass of this planet has been recently measured to be $8.4 \pm 2.1 M_\oplus$ (Almenara et al. 2015), somewhat higher than the tabulated value we used in our investigation. This increased mass would decrease the scale height, decrease the SNR of transmission spectral features, and worsen the derived abundance precisions by roughly 40%.

Table 3
Planetary Atmosphere Molecular Volume Mixing Ratios

Planet Type	Composition	H_2O	CH_4	CO	CO_2	NH_3	N_2
Hot Jupiter	1× Solar	4.27E-4	1.00E-9	4.27E-4	1.26E-7	3.16E-10	5.75E-5
Warm Neptune	1× Solar	7.24E-4	4.27E-4	1.00E-9	3.16E-11	3.16E-5	2.51E-5
Warm Neptune	1000× Solar	2.51E-1	1.00E-1	1.00E-2	1.45E-1	5.01E-5	4.47E-2
Warm Sub-Neptune	Solar	7.24E-4	4.26E-4	1.00E-9	3.16E-11	3.16E-5	2.51E-5
Warm Sub-Neptune	1000× Solar	3.98E-1	1.26E-1	1.00E-3	1.26E-1	5.01E-5	5.01E-2
Cool Super-Earth	1× Solar	7.24E-4	4.27E-4	1.00E-11	1.00E-11	1.00E-4	1.58E-5
Cool Super-Earth	100% H_2O	1.00E00	0	0	0	0	0

Note. — All mixing ratios are assumed constant with altitude and are thermochemical equilibrium values for the planet temperatures and compositions given in Tables 1 and 2 except the Hot Jupiter terminator temperature of 1200 K (Moses et al. 2011) was used instead of its Table 2 $T_{\rm eq}$ value.

clude them because their degeneracy with the absorbers at near-IR wavelengths could potentially influence the retrieved abundances (e.g., Benneke 2015; Kreidberg et al. 2015). Figure 2 shows the spectra for all planets modeled in transmission (see also Table 1).

The emission spectrum model requires 10 free parameters (5 of which are the molecular absorbers). We assume a thermally and chemically homogenous dayside, represented by a single 1D T-P profile. Because thermal emission spectra contain temperature "profile" information, we use a 5 parameter double-gray analytic formula (Line et al. 2013a, and references therein). We assume cloud-free emission spectra. Although clouds can dominate transmission spectra, they may have a lessened impact on emission spectra due to their reduced effective optical depths (Fortney 2005). The specific impact of clouds on emission spectra depends on where (at what pressure) the thermal emission arises within the atmosphere, where clouds form (i.e., where their material condensation curves cross atmospheric T-P profiles), and the absorption and scattering properties of all clouds within the pressure region probed by the emission. This is complex enough to warrant its own investigation, and we do not explore the impact of clouds on emission spectra in this work. HST WFC3 dayside spectra of several hot Jupiters are consistent with cloud-free atmospheres (McCullough et al. 2014; Stevenson et al. 2014; Kataria et al. 2015), so we do know that clouds do not suppress spectral features in emission spectra of all planets. Figure 3 shows the spectra of all planets modeled in emission (see also Table 1).

More complicated atmospheric processes such as ver-

tical mixing, atmospheric dynamics, photochemistry, ion chemistry (both photochemical and thermal), unknown cloud processes, and perhaps many other known or unknown processes (all active areas of research) could make our chosen parameter values less than realistic. Certainly any of these processes could be modeled with a nearly infinite number of unknown parameters. However, we are only investigating the impacts of the spectral (wavelengths and resolutions) and noise properties of JWST instruments on retrieving information from their observations. Therefore these assumptions are perfectly appropriate for this task of assessing the uncertainties of retrievals and any systematic deviations from the adopted forward models. We will use these parameters and their constraints to evaluate the expected JWST performance.

We assume a uniform or uniform-in-log priors[9] for the gases and other parameters, as done in Line et al. (2014b), Stevenson et al. (2014), and Kreidberg et al. (2014b). The retrievals are initialized at the true parameter vector to minimize burn-in and to speed convergence.

4. SIMULATED JWST SPECTRA

We have chosen to simulate the $\lambda = 1 - 11$ μm transmission and emission spectra of the modeled systems. This region of the spectrum shows the dominant absorption features for the major carbon-, oxygen-, and nitrogen-bearing species. We do not focus on constraining alkali metals and metal oxides/hydrides in this investigation. These species (for hot planets), along with molecular Rayleigh scattering and possible hazes, will dominate the spectrum below 1 μm.

We now describe our simulations of JWST spectra of the planetary system forward models described in §2 (Tables 1 and 2) and §3. As described in Beichman et al. (2014), all 4 JWST science instruments have spectroscopic modes that will likely be useful for observing transiting planets. Additional information on expected instrument performance and spectroscopic observations of transiting planets have been published for all instruments: NIRISS (Doyon et al. 2012), NIRSpec (Ferruit et al. 2014; Batalha et al. 2015), NIRCam (Greene et al. 2007), and MIRI (Kendrew et al. 2015). The flexible capabilities of its instruments will allow JWST users to often chose between more than one instrument mode for obtaining a spectrum of a given wavelength range. As noted in §1, large spectral range, low-to-moderate spectral resolution ($R \equiv \lambda/\delta\lambda \gtrsim 35$) observations with high spectro-photometric precision have provided the best scientific constraints on transiting exoplanet atmospheres to date. Slitless spectra with good spatial sampling and stable detectors have provided the best spectro-photometric precision (e.g., HST WFC3 G141 mode as in Kreidberg et al. 2014a).

We have chosen to simulate $\lambda = 1 - 11$ μm transmission and emission spectra of the modeled systems for the instrument modes listed in Table 4. We selected these modes because they best meet the criteria noted above: large simultaneous wavelength coverage, adequate spectral resolution ($R \gtrsim 100$), slitless operation, and bright limits sufficient to observe the selected systems with high throughput. They also have the best spatial sampling available on JWST over their wavelength ranges; good sampling should minimize systematic errors due to intrapixel response variations in the presence of pointing jitter (e.g., Deming et al. 2009). The NIRSpec instrument can also obtain spectra of bright objects over the same wavelengths as NIRISS SOSS and the NIRCam LW grisms (also in 3 exposures), and its use in exoplanet transit observations have been well studied (e.g., Ferruit et al. 2014; Batalha et al. 2015; Beichman et al. 2014). However, we chose to simulate NIRISS and NIRCam over $1 - 5$ μm wavelengths because of their slitless operation, finer spatial sampling (64 vs 100 mas / pixel), and brighter flux limits (important for the best targets).

4.1. *Signals and Random Noise Components*

Signals and noise of transmission and eclipse spectra were estimated for each instrument mode (Table 4) for each planetary system (Table 1). We combined these synthetic spectra to mimic the observational sequence of observing a single transit or eclipse event with each instrument mode (a total of 4 events for each transit or eclipse), producing a complete simulated $\lambda = 1 - 11$ μm spectrum and error bars estimating the uncertainty in each spectral channel.

We computed signals for the separate stages of a transit or eclipse event: star only or star + planet. Model stellar flux spectra were constructed by interpolating Nextgen (Hauschildt et al. 1999) models with surface gravities and effective temperatures spanning the observed values for each system. The in-transit star + planet flux was defined as $F(*+p)_{Tr,\lambda} = F_{*,\lambda} \times (1-(R_{p,\lambda}/R_*)^2)$. The star + planet emission flux is simply the sum of the model star flux and the model planet flux (see §3) at each wavelength, $F(*+p)_{Em,\lambda} = F_{*,\lambda} + F_{p,\lambda}$. Estimated detected signals of each of these astrophysical events were computed for each system using the chosen system parameters (Table 4), with

$$S_\lambda = F_\lambda A_{tel} t \frac{\lambda^2}{hcR} \tau \quad (2)$$

where S_λ is the signal per spectral element in electrons, F_λ is the star or star + planet spectral flux density, t is the total exposure time during the event, λ is the wavelength of the spectral element, R is the resolution of the spectral bin, A_{tel} is the area of the JWST aperture (25 m^2), and τ is the total system transmission (photon conversion efficiency) at that wavelength. Total exposure time t was calculated as the sum of the photon collecting time of all integrations that are executed during 0.9 $\times$ the event duration (T_{14} in Table 2). Individual integration times were computed from the host star brightnesses (Table 2) and the correlated double sample minimum integration times and bright limits of each instrument mode (c.f. Beichman et al. 2014), including the resulting readout efficiency.

We assumed that the star would also be observed for time t before and / or after the transit or eclipse event, yielding total integration time $2t$ for the visit. The system transmission τ was computed to be the product of the 3 element JWST telescope (set to 0.9) and the selected instrument. NIRISS single object slitless

[9] We have also experimented with the centered-log transform (Benneke & Seager 2012) for both solar and high mean molecular weight atmospheres and found no significant qualitative differences

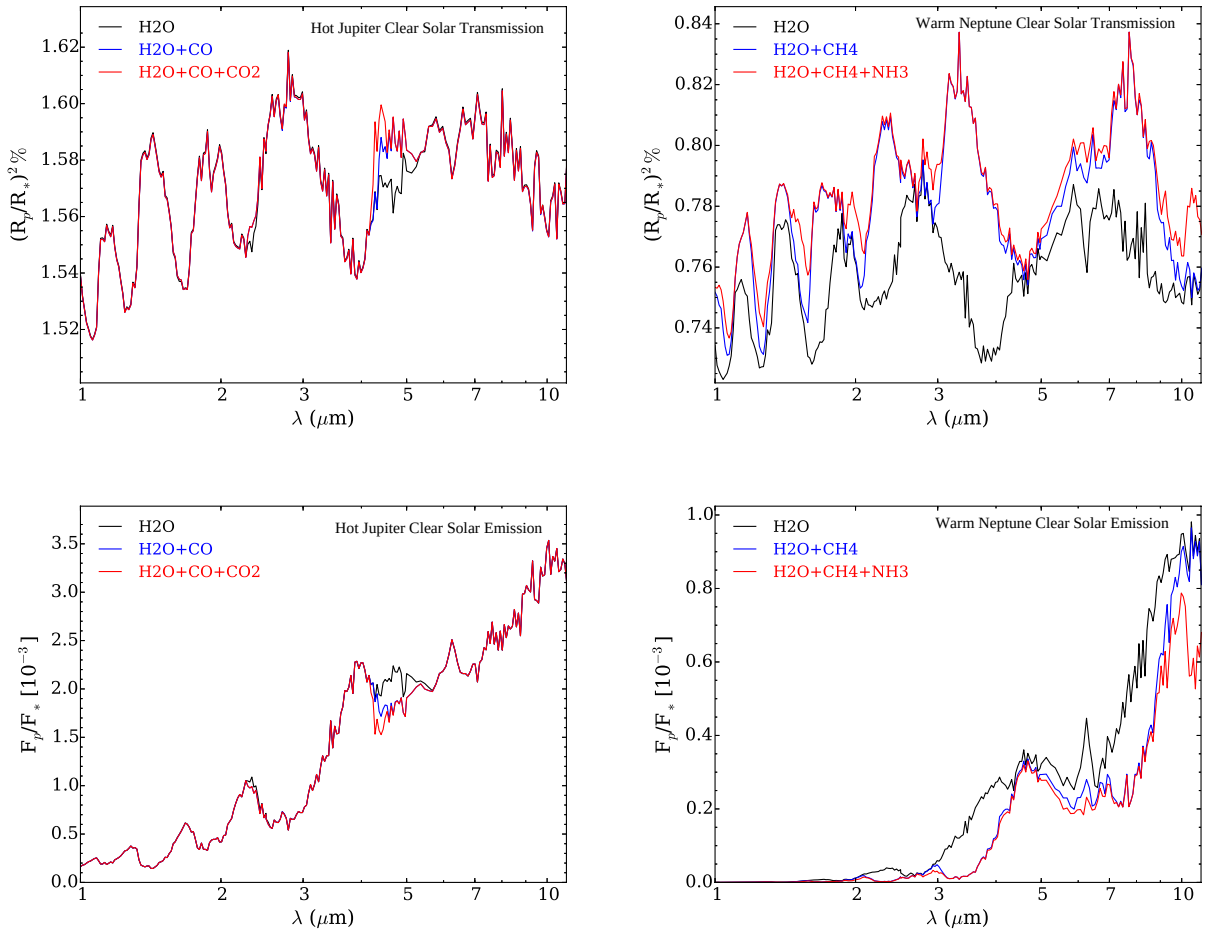

Figure 1. Left: Magnitude of absorption for specific gases for the clear solar composition hot Jupiter transmission (upper left) and emission (lower left) models. Right: Wavelengths and amplitudes of gaseous absorptions for the clear solar composition warm Neptune transmission (upper right) and emission (lower right) models. Each panel shows the impact of the dominant molecules in each model.

Table 4
Selected JWST Instrument Modes

Instrument	Mode	Optics	$\lambda(\mu m)$	Native R[a]	Sampling (pixels)[b]
NIRISS	bright SOSS	GR700XD	1 – 2.5[c]	~ 700	$\sim$25
NIRCam	LW grism	F322W2	2.5 – 3.9	~ 1700	~ 2
NIRCam	LW grism	F444W	3.9 – 5.0	~ 1700	~ 2
MIRI	SLITLESS	LRS prism	5.0 – 11[d]	~ 100	~ 2

[a] Spectral resolution $R \equiv \lambda/(\delta\lambda)$.
[b] Spatial extent of point source spectrum in pixels.
[c] Total NIRISS SOSS mode wavelength coverage spans $\lambda = 0.6 - 2.8$ μm, but we adopt the 1.0 μm short wavelength cutoff that is required for these bright stars and a 2.5 μm long wavelength cutoff to avoid spectral contamination.
[d] We adopt a long-wavelength cutoff of 11 μm for the MIRI LRS because its transmission and SNR are degraded at longer wavelengths (see Figs. 8 and 9 of Kendrew et al. 2015).

spectroscopy (SOSS) transmission τ was estimated to be 0.35 at $\lambda = 1.25\mu$m, falling off gradually at longer and shorter wavelengths in an approximation of the first order blaze function of its new GR700XD grism. Similarly, the NIRCam was estimated to have $\tau = 0.30$ at the 3.7μm blaze peak of its grisms, falling off at longer and shorter wavelengths in an approximation of the first order grism blaze function (Greene et al. 2007). The slitless photon conversion efficiency curve ($\tau \simeq 0.3$) in Figure 9 of (Kendrew et al. 2015) was adopted for the MIRI LRS τ values.

The JWST observatory is expected to have minimal natural (zodiacal) and telescope background emission at near-IR wavelengths, but the telescope background will increase quickly at wavelengths $\lambda \gtrsim 10\mu$m. Background emission can become an important noise term when observing faint stars with the MIRI LRS because its slitless

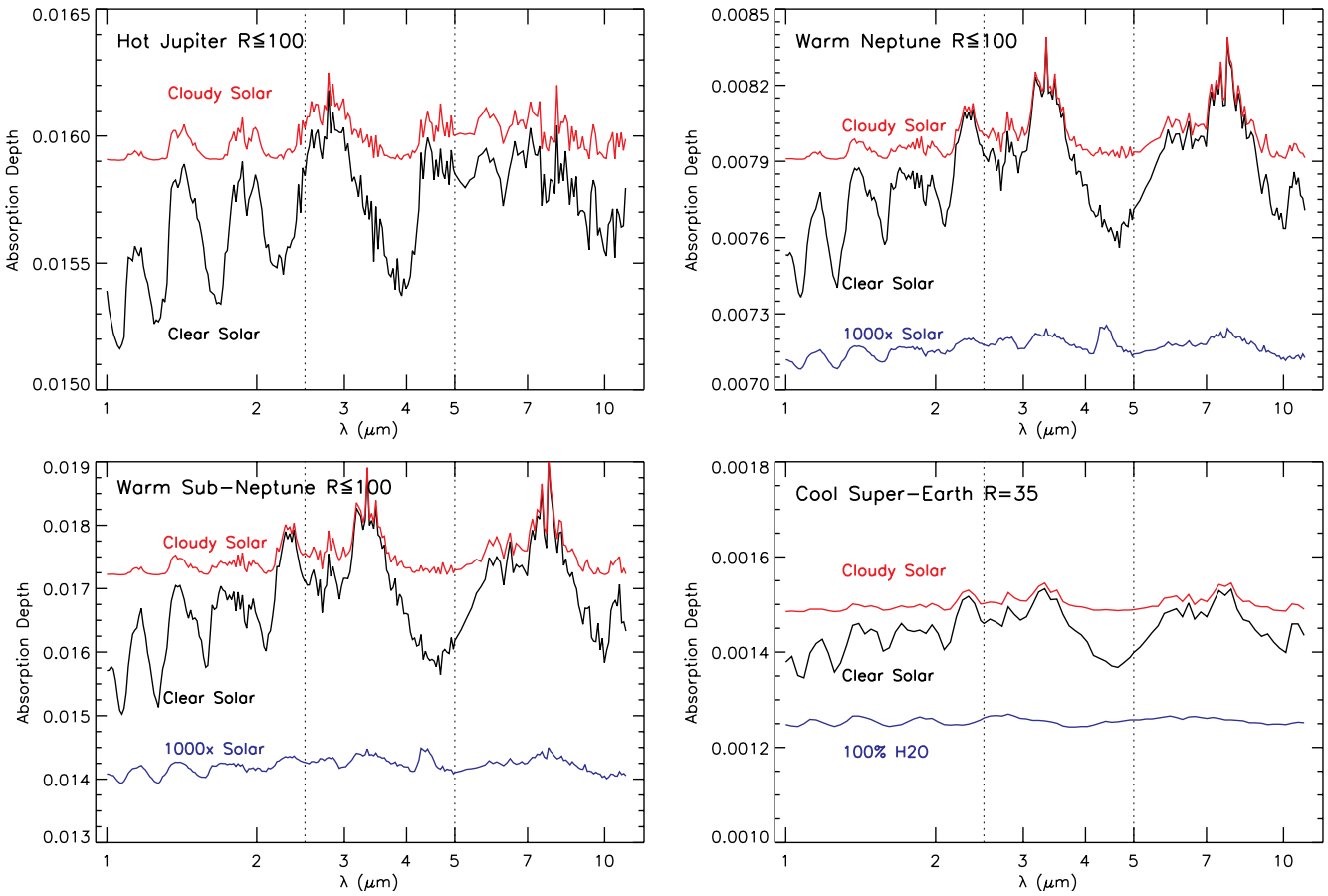

Figure 2. Forward model transmission spectra of all planets in Table 1 where Absorption Depth = $(R_{p,\lambda}/R_*)^2$. Spectra have been binned to resolution $R \leq 100$ (hot Jupiter, warm Neptune, warm sub-Neptune; see §4.2) or $R = 35$ (cool super-Earth) to match that shown for the simulated JWST data. Dashed lines show the wavelength range boundaries of the chosen NIRISS, NIRCam, and MIRI instrument modes. The vertical offsets in the cloudy spectra are due to increased opacity from opaque clouds, increasing the effective planetary radii (e.g., see Brown 2001). The smaller absorption depths of the high mean molecular weight atmospheres are due to their smaller (than solar composition) scale heights.

mode detects the full background of its $\lambda = 5 - 12\mu$m bandpass. We computed the background signal for each observation with the equation

$$Bkg = BtA_{pix}n_{pix}R_{native}/R \quad (3)$$

where Bkg is the background signal detected in each spectral bin, B is the background of the instrument mode in electrons arcsec^{-2} per second, t is the total exposure time during the event, A_{pix} is the area subtended by each pixel in arcsec^2, n_{pix} is the number of spatial x 2 spectral pixels summed in each R_{native} native 2-pixel resolution element of the selected observing mode, and R is the final binned spectral resolution of the observation. The B background values were computed from the average zodiacal and telescope backgrounds of each instrument mode provided by the STScI JWST prototype exposure time calculator[10].

Noise values were computed at each wavelength as the sums of photo-electron Poisson noise, background Poisson noise, and total (read and dark) detector noise $N_{d,tot}$:

$$N_\lambda = \sqrt{S_\lambda + Bkg + N_{d,tot}^2} \quad (4)$$

[10] http://jwstetc.stsci.edu/etc/

where

$$N_{d,tot} = N_d\sqrt{n_{pix}n_{ints}R_{native}/R}. \quad (5)$$

N_d is the total (read and dark current) detector noise of a single integration, and n_{ints} is the number of integrations during exposure time t. We set N_d = 18 electrons for the HgCdTe detectors (NIRISS and NIRCam modes) and $N_d = 28$ electrons for MIRI; these correlated double sample noise values are expected maxima for nearly all observations. The numbers of integrations n_{ints} were set using the bright limits, efficiencies, and frame times of each instrument mode given in Beichman et al. (2014) such that the total real time fit within 0.9 times the transit duration (T_{14} in Table 2), summing to total exposure time t for the event (plus equal time on the host star alone).

4.2. *Final simulated spectra*

The signals and backgrounds of the astrophysical events were combined as follows to estimate the final

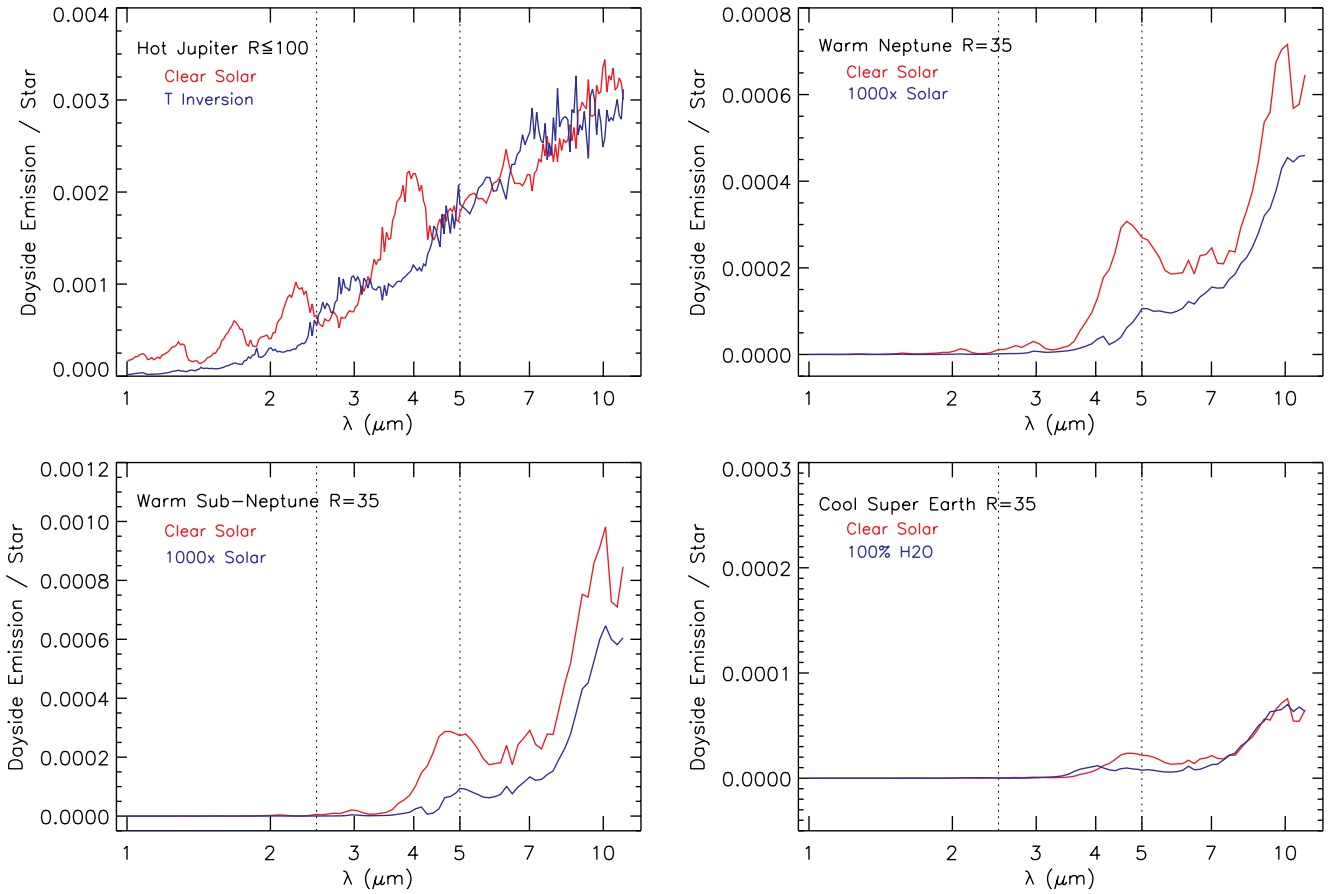

Figure 3. Forward model emission spectra of all planets in Table 1. Spectra have been binned to resolution $R \leq 100$ (hot Jupiter, warm Neptune, warm sub-Neptune; see §4.2) or $R = 35$ (cool super-Earth) to match that shown for the simulated JWST data. Dashed lines show the wavelength range boundaries of the chosen NIRISS, NIRCam, and MIRI instrument modes.

transmission (Tr_λ) and emission (Em_λ) spectra:

$$Tr_\lambda = \frac{S_\lambda(F_*) + Bkg - (S_\lambda(F(*+p)_{Tr}) + Bkg)}{S_\lambda(F_*) + Bkg - \langle Bkg \rangle} \quad (6)$$

and

$$Em_\lambda = \frac{S_\lambda(F(*+p)_{Em}) + Bkg - (S_\lambda(F_*) + Bkg)}{S_\lambda(F_*) + Bkg - \langle Bkg \rangle}. \quad (7)$$

Note that $Tr_\lambda \equiv (R_{p,\lambda}/R_*)^2$ and $Em_\lambda \equiv F_{p,\lambda}/F_*$ in noiseless cases. These Tr_λ and Em_λ signals were computed for the chosen system, instrument, and observation parameters for each planetary model in Table 1. We binned spectral channels to achieve a final resolution of $R \leq 100$ per wavelength bin; instrument modes with higher intrinsic R were binned to $R = 100$, while ones with lower R (i.e., MIRI LRS at $\lambda < 8\mu$m; see Kendrew et al. 2015) were not binned. We chose $R = 100$ as a compromise value low enough to maximize signal-to-noise while also being high enough to resolve molecular band spectral features.

We did perform a preliminary test of how binning impacts the retrieved uncertainties of H_2O, CO, and CO_2 in the hot Jupiter solar composition cloudy transmission spectrum. We found that binning $\lambda = 1 - 5\mu$m (NIRISS + NIRCam) spectra to $R = 350$ (2 NIRISS resolution elements) did not produce any mixing ratio uncertainties that were less than ones retrieved for data binned to $R = 100$ in 2 trials using different instances of $N_{d,tot}$ (no systematic noise was included). However, the ideal binning of each observing mode will likely be sensitive to actual in-flight noise performance, and this will not be known until after JWST begins operations.

The large aperture of JWST will ensure that the observatory will collect a large number of photons on bright stars, potentially resulting in the detection of $\sim 10^{10}$ or more photo-electrons per spectral bin when summing a significant number of observations of transit or eclipse events. In such cases, stellar photon noise will dominate N_λ, resulting in signal-to-noise ratios SNR $\sim 10^5$ or N_λ values being only 10 parts per million (10 ppm) of signal values. Existing observations of transiting planets have not yielded such low noise values. Either astrophysical noise (e.g., Barstow et al. 2015) and / or instrumental noise (e.g., de-correlation residuals) produce systematic noise floors that are not lowered when summing more data. The best HST WFC3 G141 observations of transiting systems to date have noise on the order of 30 ppm (Kreidberg et al. 2014a), while observations of transiting planets with the Spitzer Space Telescope Si:As detectors showed noise as low as $\sim$ 65 ppm (Knutson et al. 2009).

We adopt reasonably optimistic systematic noise floor values of 20 ppm, 30 ppm, and 50 ppm for NIRISS SOSS

($\lambda = 1 - 2.5\mu$m), NIRCam grism ($\lambda = 2.5 - 5.0\mu$m), and MIRI LRS ($\lambda = 5.0 - 11\mu$m) observations, respectively. These are less than or equal to the values estimated by Deming et al. (2009) for the JWST NIRSpec and MIRI instruments. The excellent spatial sampling of the NIRISS GR700XD SOSS grism approaches that of the HST WFC3 G141 spatial scanning mode, and both instruments have reasonably similar HgCdTe detectors. We anticipate that de-correlation techniques will continue to improve, so we assign a 20 ppm noise floor value to NIRISS even though HST has not yet done quite this well. NIRCam will have similar detectors but will not be sampled as well (see Table 4), so we assign it a systematic noise floor equivalent to HST's best performance to date. The MIRI imager / LRS detector is similar (in materials, architecture, and sampling) to the Spitzer IRAC Si:As detector used by Knutson et al. (2009), and we use this as the basis for assigning a 50 ppm noise floor to MIRI. We will not know the actual performance of these instruments until after JWST commissioning, but Beichman et al. (2014) have demonstrated decorrelated noise precision similar to the adopted NIRISS and NIRCam values in laboratory tests devised to simulate their observations of transiting planets.

A single instance of noise was computed for each transmission or emission observation, using the expression for N_λ and propagating through the relation Tr_λ or Em_λ. We then added the appropriate systematic noise floor in quadrature, using the values given above. The single noise instance was drawn from a distribution with this amplitude, and the instance was added to the Tr_λ or Em_λ signal to produce the final simulated spectrum for each planet model in Table 1. Uncertainties were set to the total noise amplitude determined for each bin; Figures 4 and 5 show the simulated spectra for each case with these uncertainties plotted as error bars for 1 example. We computed different noise instances for each instrument mode (NIRISS SOSS, NIRCam LW grism, and MIRI slitless LRS). The resultant spectra and uncertainties were then used to retrieve the parameters of each model planet's atmosphere as discussed in §3.

5. RETRIEVAL RESULTS

The retrievals were performed for the wavelength ranges of up to 3 different instrument combinations for each of the model planet atmospheres: NIRISS ($\lambda = 1.0 - 2.5$ μm), NIRISS + NIRCam ($\lambda = 1.0 - 5.0$ μm), and NIRISS + NIRCam + MIRI LRS ($\lambda = 1.0 - 11$ μm). Retrievals were performed for all 3 combinations in cases of high signal-to-noise, i.e. the transmission spectra of all planet atmospheres and the hot Jupiter emission spectra. The warm Neptune and warm sub-Neptune emission spectra had insufficient signal-to-noise for retrievals with only NIRISS ($1.0 - 2.5$ μm) data, and *the complete $\lambda = 1 - 11$ μm cool super-Earth emission spectrum had insufficient signal-to-noise for retrievals.* There simply is not enough flux contrast F_p/F_* for useful emission spectra from this system when a single secondary eclipse is observed at each wavelength. Photometric filter observations may be more useful for constraining the planet's properties. Small ($R \lesssim 2R_\oplus$), cool (T <700 K) planets will need host stars with $K \lesssim 8.5$ mag and / or spectral types later than M0 V for useful emission spectra of single secondary eclipses.

In this section, we focus on the retrieved parameters that most directly impact the simulated spectra: mixing ratios of significant molecular absorbers (CH_4, CO, CO_2, H_2O, NH_3), clouds, and atmospheric temperature-pressure (T-P) profiles. C/O (carbon-to-oxygen ratios) and [Fe/H] are *derived* (not retrieved) from these quantities by a Monte-Carlo propagation of the molecular uncertainties as in Line et al. (2013a) and Line et al. (2015), respectively.

Figures 6 – 9 summarize the marginalized posteriors for the relevant retrieved parameters and the derived C/O and [Fe/H] for the different planet and atmosphere scenarios. The input forward model true values and retrieval priors are also indicated in the figures. Any offsets between retrieved distribution medians and true values are due to the particular instance of random noise on the simulated spectra. Note that the input [Fe/H] values are slightly lower than the solar ([Fe/H]=0) and 1000× solar ([Fe/H]=3) bulk values that were used to construct the forward models (see §2). This is because some of the O atoms have been removed to account for the expected formation of Mg_2SiO_4 (enstatite) condensates in clouds in deep atmospheres below the regions probed by emission or transmission spectra (except in the Hot Jupiter)[11].

The prior distributions on the retrieved parameters are uniform-in-log. However, uniform-in-log priors bias the resulting C/O and [Fe/H] distributions (see discussion in Line et al. 2013a), thus we show what these distributions look like resulting from the uniform-in-log priors on the gas mixing ratios. These would be the distributions obtained had we made no observations. Therefore these prior-derived distributions must be considered in interpreting the posterior log (C/O) and [Fe/H] distributions.

5.1. *Impacts of Atmospheric Parameterization*

We now investigate whether the chosen atmospheric parameterization and priors may impact the retrieved results. Kreidberg et al. (2015) used both the "free" and "chemically consistent" retrieval approaches to determine the C/O in the transmission spectrum of WASP-12b. They found consistent results amongst the two approaches suggesting a robust solution. We perform a similar analysis here. In addition to retrieving the mixing ratios of the individual molecules independent of the chemistry that links them (the "free" approach performed thus far), we also retrieve log C/O and [Fe/H] directly as a test case (with prior ranges from -2 to 2, and -4 to 4 respectively). These quantities, together with the temperature and pressure at each level in the atmosphere, permit the determination of the thermochemical equilibrium gas mixing ratios. These solutions are advantageous as they are chemically plausible and thermochemically self-consistent. However, such an approach does not account for the nearly limitless possible combinations of physical and chemical processes occurring in planetary atmospheres (e.g., vertical mixing, photochemistry, ion chemistry, 3-D transport, cloud-gas microphysics interactions, interior-atmosphere chemistry coupling, escape processes, non-LTE, etc.) so we have not adopted it as our primary technique.

[11] Also, the true metallicities for the emission spectra are slightly lower than for transmission as we did not include N_2 in the total metallicity calculation

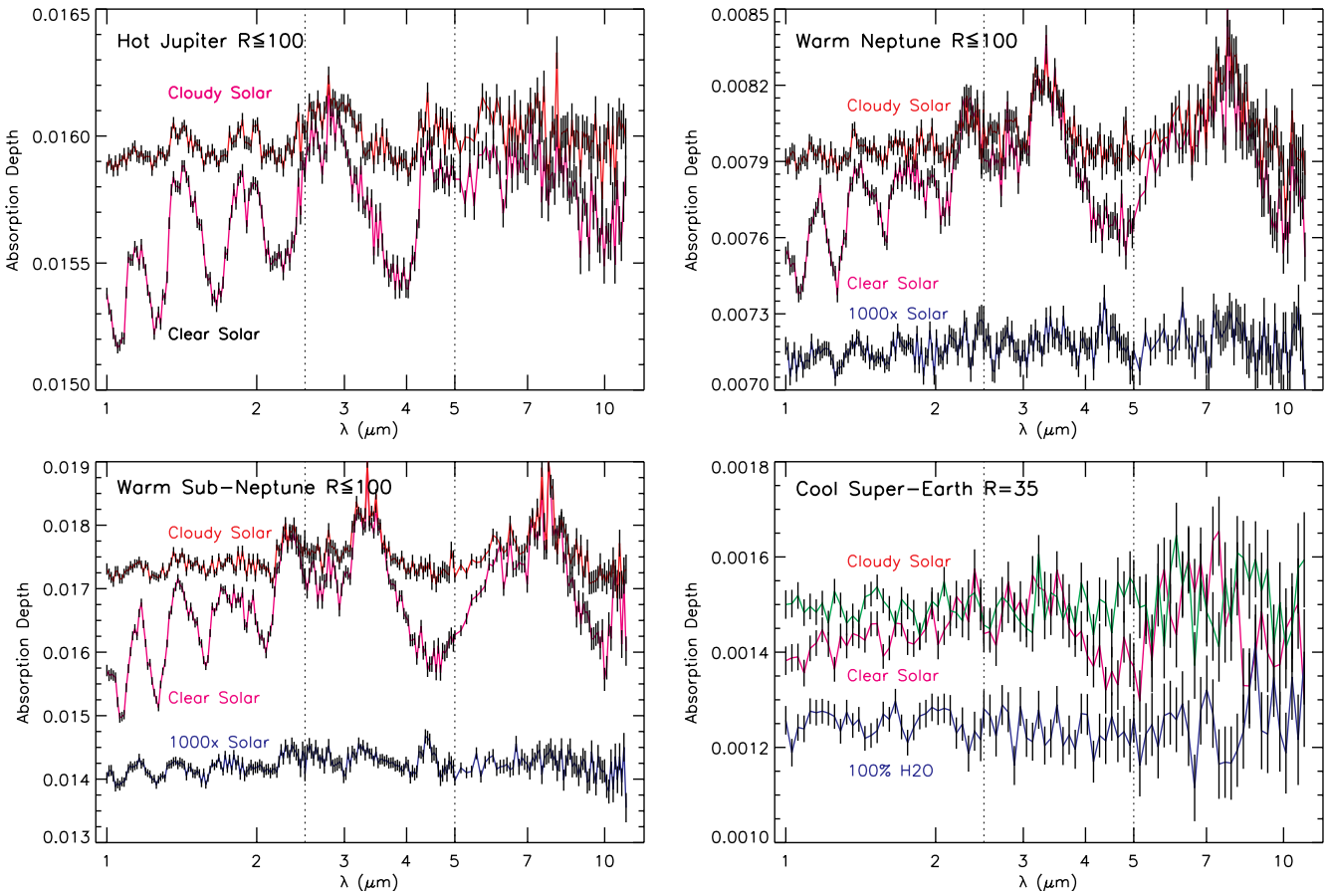

Figure 4. Final simulated transmission spectra of the transmission models shown in Fig. 2. The $Tr_\lambda = (R_{p,\lambda}/R_*)^2$ spectra are for a single transit with equal time on the star alone for each of the 4 instrument modes (Table 4). Spectra have been been binned to resolution $R \leq 100$ (hot Jupiter, warm Neptune, warm sub-Neptune; see §4.2) as used for all retrievals or $R = 35$ (cool super-Earth) for display purposes only. The simulated spectra include a noise instance and are presented as colored curves. The black error bars denote 1σ of noise composed of random and systematic components. Dashed lines show the wavelength range boundaries of the chosen NIRISS, NIRCam, and MIRI instrument modes.

While not comprehensive, we perform one example using this chemically consistent approach and examine the impact it has on our ability to infer the atmospheric metallicity and C/O ratio. We retrieve on the full $1-11$ μm wavelength warm sub-Neptune emission spectrum for the clear solar composition atmosphere. Figure 10 illustrates the resulting marginalized log(C/O) and [Fe/H] metallicity posteriors compared with those *derived* from the molecular abundances in our baseline free retrievals (i.e., Fig. 8, top row). The C/O histograms are qualitatively similar; both suggest a weak constraint of the C-to-O ratio. Perhaps more interesting is the comparison of the metallicity histograms. The chemically consistent approach provides a several-orders-of-magnitude better metallically constraint than that derived from retrieving the molecular mixing ratios freely. This is because the chemically consistent approach rules out combinations of molecular abundances that do not abide by thermochemical equilibrium. Effectively, more prior information is being added to the chemically consistent retrieval system in the form of a more sophisticated parameterization with more assumptions but with fewer free parameters. More generally, it would be possible to apply chemically consistent models on all posterior "free" retrieval histograms (Figures 6 – 9) to rule out non-physical parameter spaces within the equilibrium framework. This would be an intermediate step between the classic retrieval and forced self-consistency, but we do not implement it here.

Given a high enough signal-to-noise ratio and sufficient spectral resolution along with correct physics and chemistry constraints, one would expect the two approaches to produce the same distributions of the retrieved quantities. That would suggest true independence from any prior assumptions, and this would be the ideal regime for learning more about these atmospheres.

5.2. *Temperature-Pressure Profiles and Parameter Uncertainties*

Figure 11 shows the range of T-P profiles retrieved from the simulated emission spectra over the 3 different wavelength ranges. Figure 12 shows normalized thermal emission contribution functions for the solar composition hot Jupiter and warm sub-Neptune planets to illustrate where their thermal emissions originate. The solar composition warm Neptune contribution function is very similar to the warm sub-Neptune one.

Table 5 lists the the 68% confidence intervals of the retrieved parameters of the transmission and emission scenarios (see §3, Table 1). For cases in which a molecule is not particularly abundant (e.g., CH_4 in the hot Jupiter

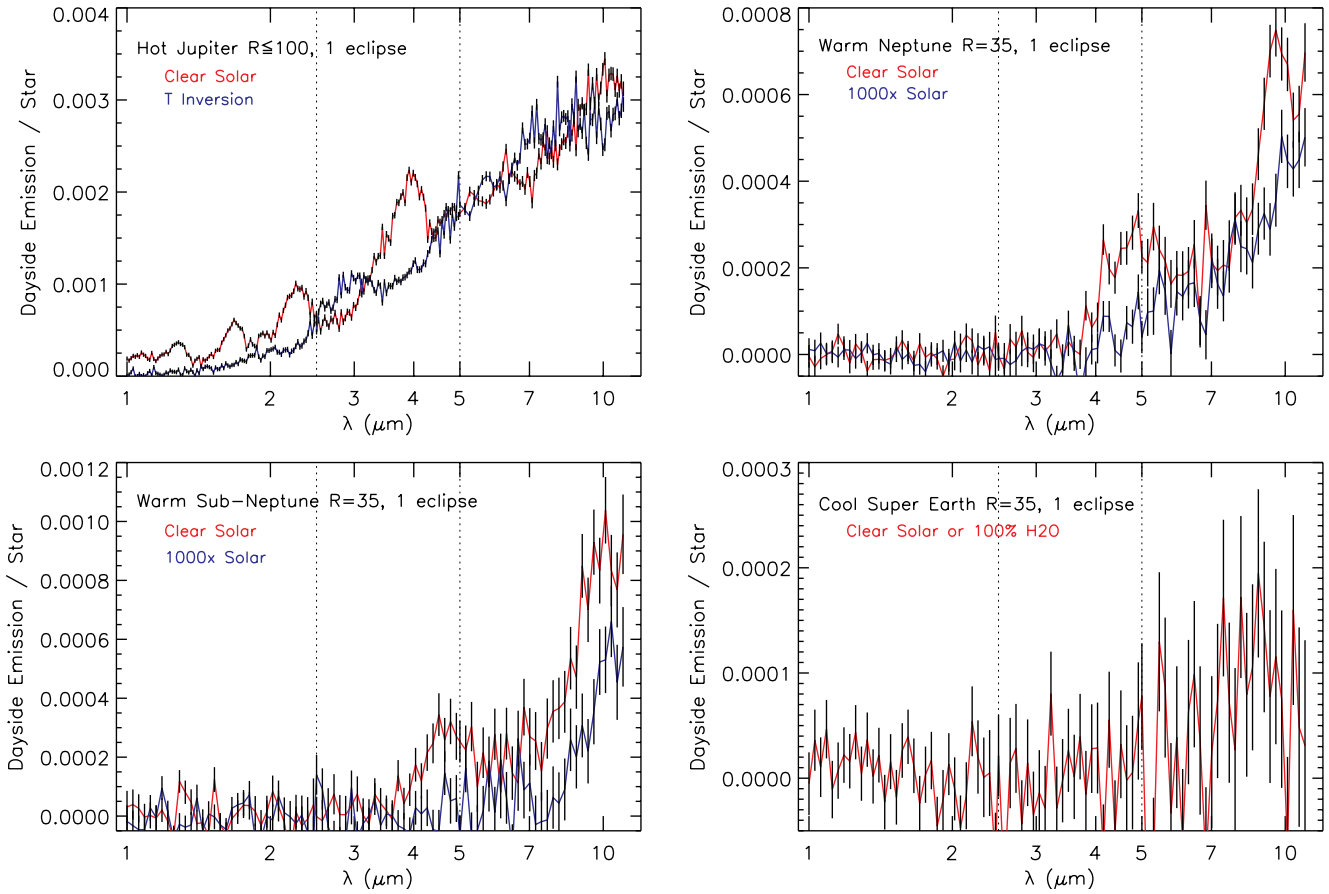

Figure 5. Final simulated spectra of the emission models shown in Fig. 3. The $Em_\lambda = S(F_p)/S(F_*)$ spectra are for a single eclipse with equal time on the star alone for each of the 4 instrument modes (Table 4). Spectra have been been binned to resolution $R \leq 100$ as used for all retrievals (hot Jupiter; see §4.2) or $R = 35$ for display purposes only (warm Neptune, warm sub-Neptune, cool super-Earth). The simulated spectra include a noise instance and are presented as colored curves. The black error bars denote 1σ of noise composed of random and systematic components. Dashed lines show the wavelength range boundaries of the chosen NIRISS, NIRCam, and MIRI instrument modes. Only 1 model is shown for the cool super-Earth for clarity; the noise is much greater than the difference between the clear solar and 100% H_2O atmospheres.

and CO or CO_2 in the cooler objects), only upper limits could be obtained. We quote the 3σ upper limits instead of confidence widths in these case. We caution however, that many of these upper limits are relatively soft and that one should really look at the histograms to get a sense for the distribution.

These numbers are meant to be a guide to illustrate how the constraints change from one object to the next. We also note that there is typically a ∼10% uncertainty on these uncertainty values due to the particular instances of random noise applied. In the remainder of this section, we examine how well the directly retrieved parameters constrain the different planetary atmospheres.

5.3. *Transmission Spectra Constraints*

Figures 6 – 9 and Table 5 show that the mixing ratios of the dominant molecules for a particular planet type are well constrained (bounded posterior rather than an upper limit) in the transmission spectra of all clear solar atmospheres in most cases. Furthermore, observations with NIRISS alone ($\lambda \leq 2.5$ μm) can constrain H_2O in these atmospheres nearly as well as observations out to 11 μm wavelengths in some cases. For example, Table 5 shows that the retrieved H_2O mixing ratio of the clear solar hot Jupiter has a 68% uncertainty of 0.16 dex (45%) for a $\lambda = 1 - 11$ μm spectrum, and this degrades to only 0.20 dex (58%) when only using the $1 - 2.5$ μm wavelengths in a NIRISS observation. However, CO is well constrained (uncertainty $\sim$ 0.3 dex for retrievals done with the full $1 - 11$ μm or $1 - 5$ μm spectra, but the uncertainty is much worse ($\sim$ 1.8 dex) when only the NIRISS data are used.

The H_2O and CH_4 uncertainties of the warm Neptune clear solar atmosphere increase by ∼0.3 dex (factor of ∼2), providing uncertainties of ∼1 dex (factor of ∼10) when using only the NIRISS wavelengths. These species have similar NIRISS-only uncertainties in the warm sub-Neptune clear solar atmosphere, but their full $\lambda = 1 - 11$ μm spectra provide better uncertainties (∼0.2 vs ∼0.5 dex for the warm Neptune). These values are about ∼1.5 dex for the full $1 - 11$ μm wavelengths for the cool super-Earth clear solar atmosphere, and the CH_4 uncertainty does not change much when only considering the NIRISS data range. However, the retrieved H_2O mixing ratio value becomes an upper limit. Overall it is encouraging that these atmospheres can be constrained so well in these modest observations (1 transit at each wavelength), and the wavelength range of NIRISS alone

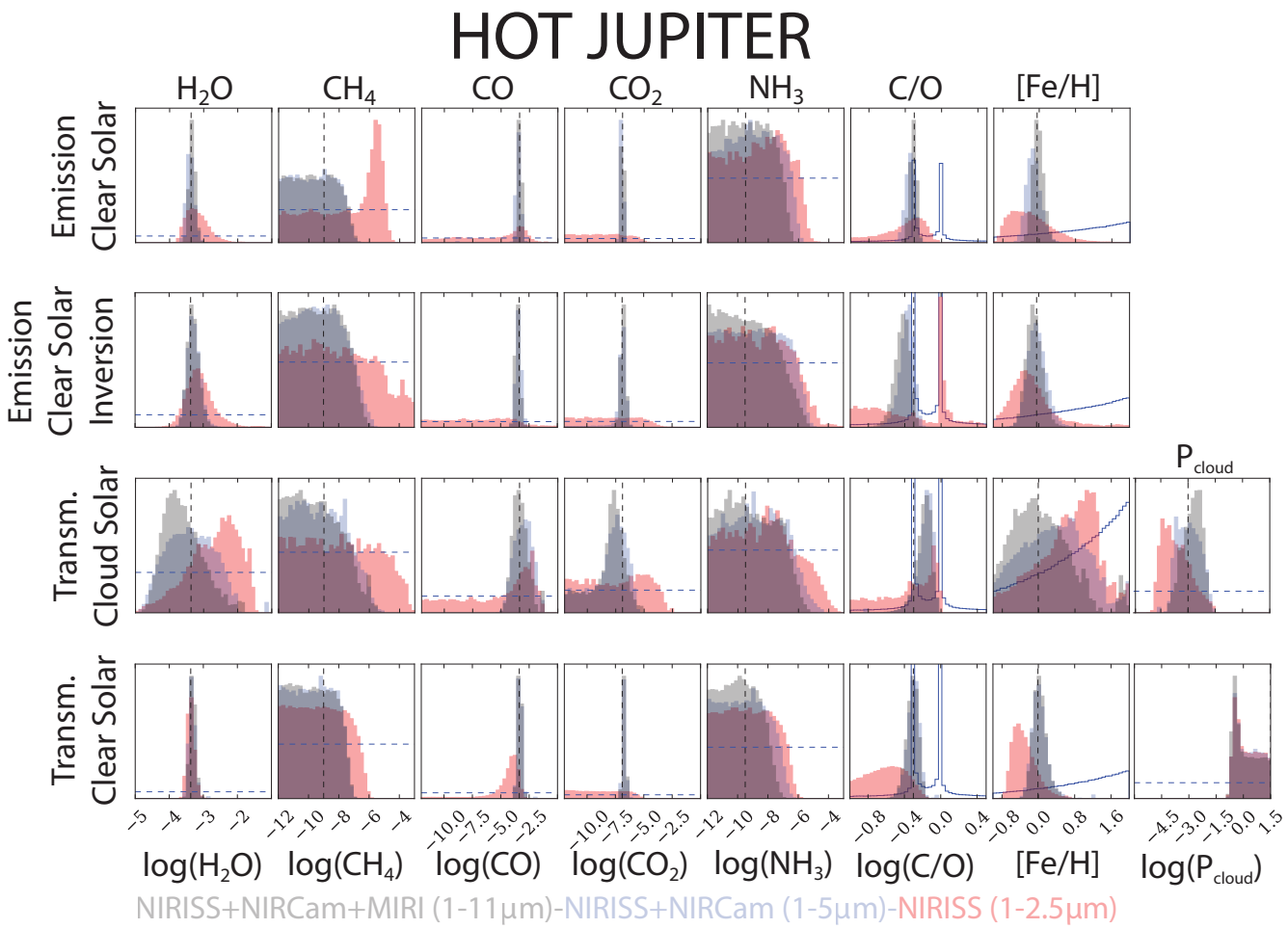

Figure 6. Retrieved and derived quantities of the hot Jupiter planet. Retrieved volume mixing ratios are shown for each molecular species. Marginalized posterior histogram shadings are color coded by instrument mode and therefore wavelengths of spectra used for retrievals. Priors are indicated by blue horizontal dashed lines for the retrieved molecules. The resulting distributions for the derived quantities log (C/O) and [Fe/H] from the gas priors are more complex distribution functions (shown in blue). True values are indicated by vertical dashed black lines for all quantities.

is sufficient to detect dominant species with good confidence or even measure mixing ratios to good precision in some cases (i.e., the chosen hot Jupiter). Even for gases that are not abundant in the atmospheres (CH_4 and NH_3 in the hot Jupiter, CO and CO_2 in the cooler objects) relatively low upper limits can be obtained. For instance, most scenarios within the hot Jupiter planet type can detect, or rather, rule out NH_3 and CH_4 at the $\sim$ 1 ppm level.

Planets with cloudy atmospheres will be more challenging to constrain with transmission spectra; this is already apparent from numerous HST observations of GJ 1214b (e.g., Kreidberg et al. 2014a; Croll et al. 2011, and references therein) and other planets that exhibit weak or no spectral features. Figures 6 – 9 and Table 5 show that the mixing ratios of most molecules are not constrained well (uncertain by more than 1.0 dex) with $\lambda \leq 2.5$ μm (NIRISS only) transmission spectra for solar composition exoplanet atmospheres with clouds. Mixing ratio uncertainties improve somewhat when $\lambda \geq 5$ μm data (NIRCam or NIRCam+MIRI) are added in many cases. However, the resulting constraints are considerably worse than those of the clear solar atmospheres (as good as 0.2 – 0.5 dex as discussed above). Mixing ratio uncertainties improve to $\sim$1 dex for some molecules in the hot Jupiter and warm sub-Neptune cloudy atmospheres when these longer wavelengths are also included in the retrievals. The mixing ratio uncertainties of the molecules in the warm Neptune system also improve with these longer wavelength retrievals, but none get close to 1.0 dex. The cool super-Earth system retrievals only produce molecular mixing ratio limits for the cloudy atmosphere case regardless of wavelength range used.

Cloud-top pressure P_{cloud} is also retrieved for the transmission cases, and Table 5 shows that this is constrained to $\sim$1 dex for the hot Jupiter and warm sub-Neptune systems when using complete $\lambda = 1 - 11$ μm spectra of cloudy solar atmospheres. This allows locating the position of clouds to an order of magnitude in pressure in their atmospheres. Reducing the wavelength range to $1 - 5$ and $1 - 2.5$ μm increases the uncertainty to $\sim$1.4 and $\sim$1.7 dex, respectively. The warm Neptune system is not constrained quite as well (mostly due to its less favorable transmission parameters), having an uncertainty in P_{cloud} of 1.4 – 1.9 dex for the 3 different wavelength ranges of the cloudy solar atmosphere case. The

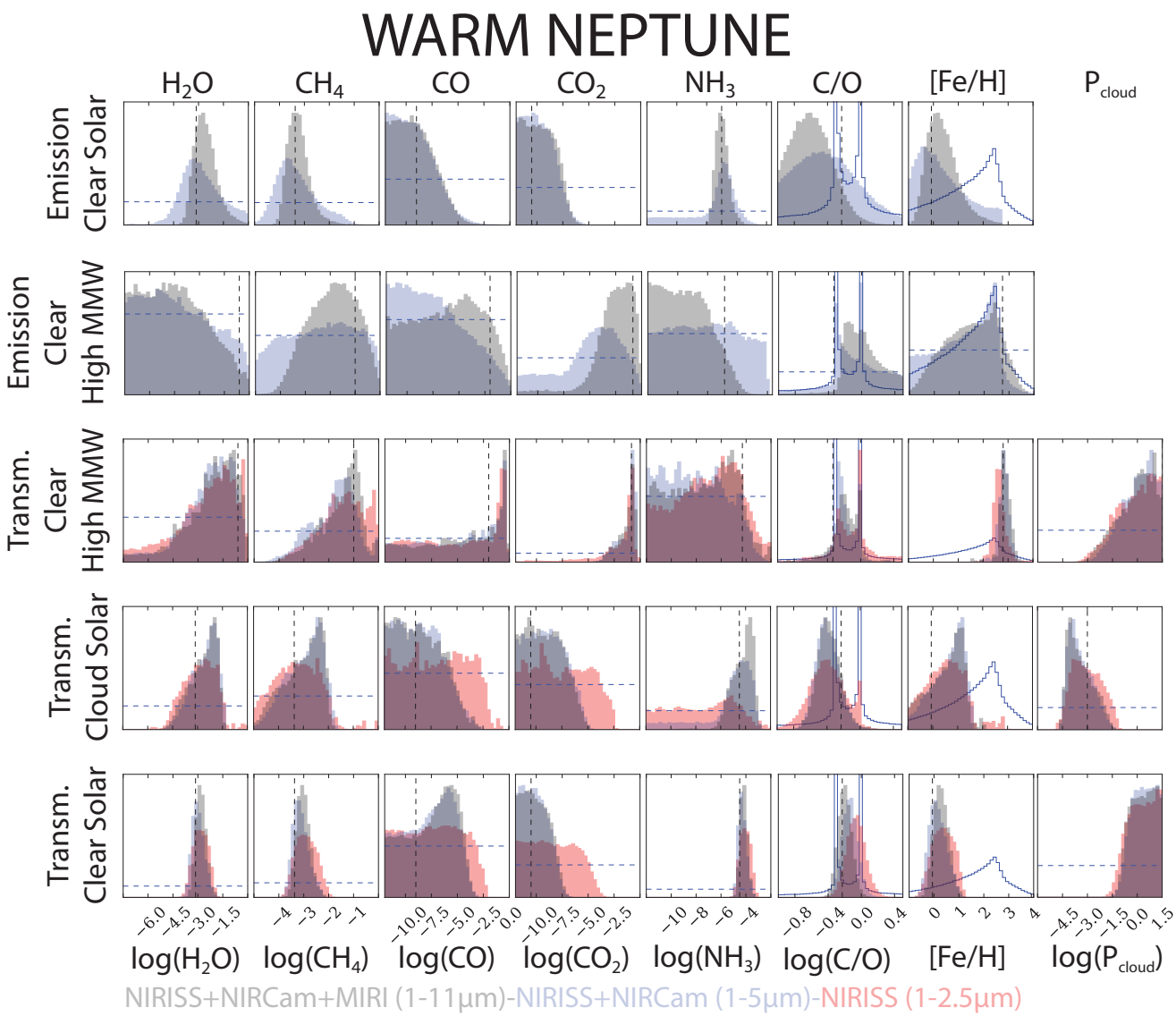

Figure 7. Retrieved and derived quantities of the warm Neptune planet. Retrieved mixing ratios are shown for each molecular species. Marginalized posterior histogram shadings are color coded by instrument mode and therefore wavelengths of spectra used for retrievals. Priors are indicated by blue horizontal dashed lines for the retrieved molecules. The resulting distributions for the derived quantities log (C/O) and [Fe/H] from the gas priors are more complex distribution functions (shown in blue). True values are indicated by vertical dashed black lines for all quantities.

retrievals provide lower limits for P_{cloud} (highest cloud altitudes) for all clear atmospheres (solar or HMMW) of the hot Jupiter, warm Neptune, and warm sub-Neptune systems. Clouds in the clear solar atmospheres of all three systems are constrained to P $\gtrsim$ 1 mbar, a useful limit given that transmission spectra probe only high altitude / low pressure atmospheric regions. P_{cloud} is not constrained well for any atmospheres of the cool super-Earth system. The P_{cloud} histograms in Figures 6 – 9 illustrate these constraints graphically.

5.4. *Emission Spectra Constraints*

Emission spectra retrievals constrain the mixing ratios of the most dominant species of the solar composition hot Jupiter (better than 0.3 dex for CO, CO_2, and H_2O) and warm Neptune (to ∼1 dex for CH_4, H_2O, and NH_3) atmospheres. Figures 6 - 9 and Table 5 show that $\lambda > 5$ μm data (e.g., MIRI) are required to obtain these good constraints. This can be understood by examining Fig. 5; emission spectra have low SNR at shorter wavelengths, and there are numerous strong molecular absorption features at $\lambda > 2.5$ μm. Note that the NIRISS-only ($\lambda = 1 - 2.5$ μm) emission spectrum of the hot Jupiter gives a false peak in its CH_4 mixing ratio, and this disappears when longer wavelength data are added (see Fig. 6). Molecular mixing ratio uncertainties are worse than ∼1 dex for the emission retrievals of the warm sub-Neptune planet, and the SNR of the emission spectrum of the cool super-Earth was too low to perform useful retrievals at any wavelengths (see also Fig. 5).

These results show that JWST $\lambda > 2.5$ μm emission spectra with moderate-to-high SNR will be very useful for atmospheric characterization. Emission spectra are also required to retrieve T-P profiles (Figure 11), particu-

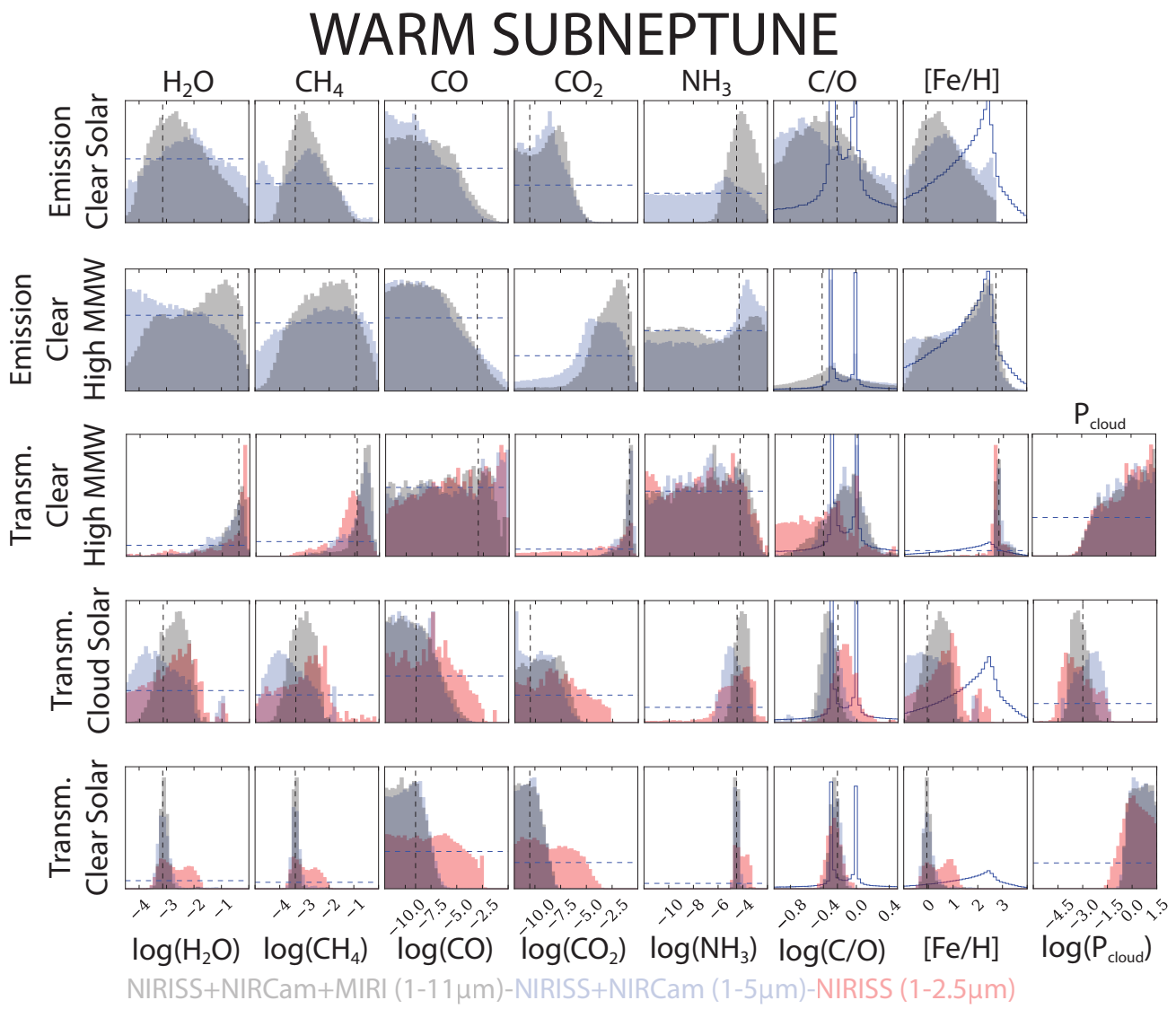

Figure 8. Retrieved and derived quantities of the warm sub-Neptune planet. Retrieved mixing ratios are shown for each molecular species. Posterior predictive histogram shadings are color coded by instrument mode and therefore wavelengths of spectra used for retrievals. Priors are indicated by blue horizontal dashed lines for the retrieved molecules. The resulting distributions for the derived quantities log (C/O) and [Fe/H] from the gas priors are more complex distribution functions (shown in blue). True values are indicated by vertical dashed black lines for all quantities.

larly important for understanding energy absorption and transport in strongly insolated atmospheres. Fortney (2005) showed that the direct, face-on geometry of emission spectra are much less impacted by clouds or hazes that the slant geometry of transmission spectroscopy observations. Therefore we assume that observations and retrievals of emission cloudy solar atmosphere emission spectra will be very similar to the clear solar composition atmosphere emission spectra studied here. Given that, retrievals of JWST $\lambda = 1 - 11$ μm emission spectra provide significantly better constraints than the transmission spectra on the mixing ratios of most molecules for cloudy hot Jupiter and warm Neptune atmospheres (see Table 5). Each star+planet system should be evaluated to determine whether emission or transmission observations are more favorable for detecting spectral features and constraining parameters of interest via atmospheric retrievals. It would be ideal to acquire and combine both transmission and emission spectra to probe planetary atmospheres over the broadest possible pressure range and to use all data to constrain compositions and chemistries (Griffith 2014; Kreidberg et al. 2014b).

Spectral absorption features are clearly suppressed over the entire $\lambda = 1 - 11$ μm wavelength range of the hot Jupiter temperature inversion emission spectrum (Fig. 5), and the inversion is detected at modest to high SNR in the retrievals. As shown in Fig. 11, the temperatures of the hot Jupiter atmosphere decreases to $T = 1260$ K at $P = 10^{-2}$ bar, and then increases to $T = 2100$ K at $P = 10^{-4}$ bar for the inversion model. This difference of $\Delta T = 840$ K is detectable in the retrieved T-P profiles of all 3 wavelength ranges. At these pressures, the 1 σ temperature uncertainties of the $1-2.5$, $1-5$, and $1-11$ μm wavelength ranges are approx-

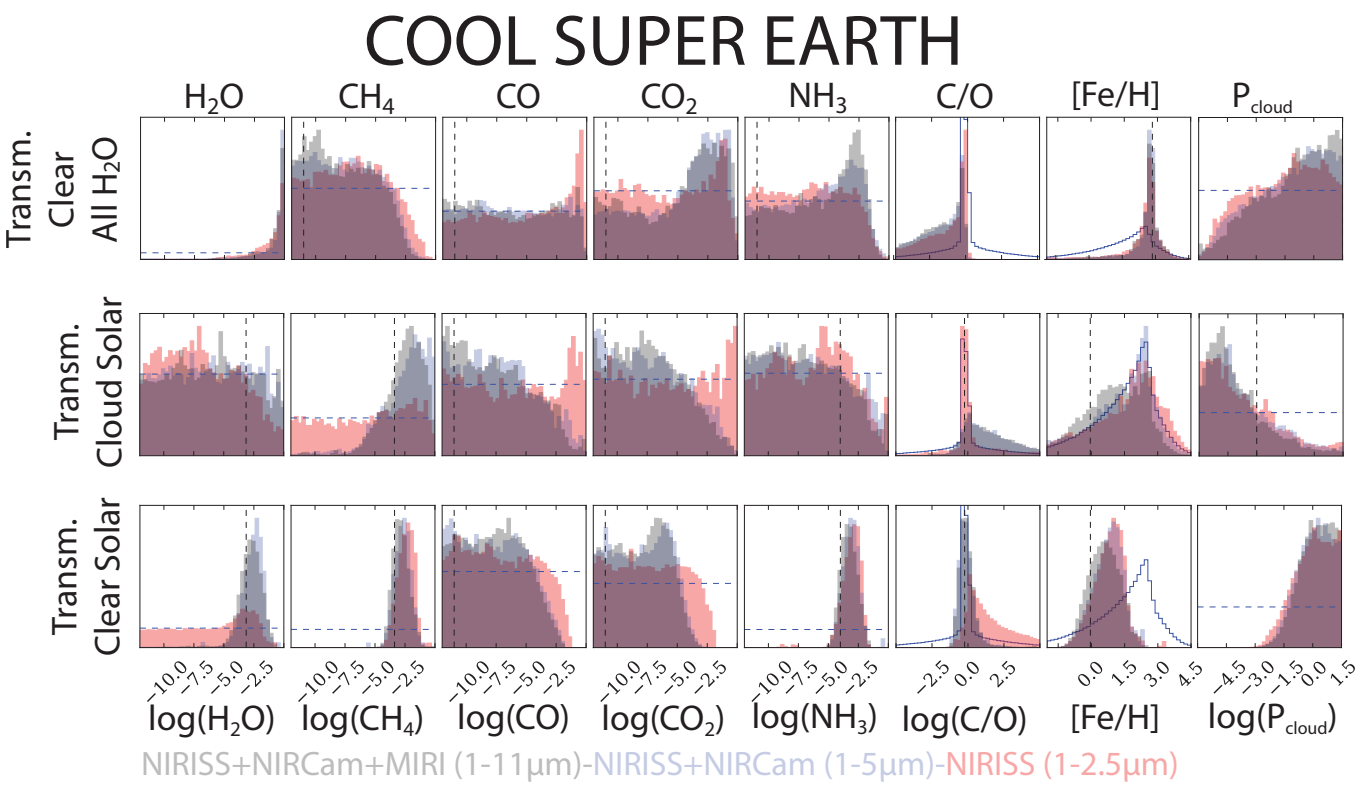

Figure 9. Retrieved and derived quantities of the cool super-Earth planet. Retrieved mixing ratios are shown for each molecular species. Posterior predictive histogram shadings are color coded by instrument mode and therefore wavelengths of spectra used for retrievals. Priors are indicated by blue horizontal dashed lines for the retrieved molecules. The resulting distributions for the derived quantities log (C/O) and [Fe/H] from the gas priors are more complex distribution functions (shown in blue). True values are indicated by vertical dashed black lines for all quantities.

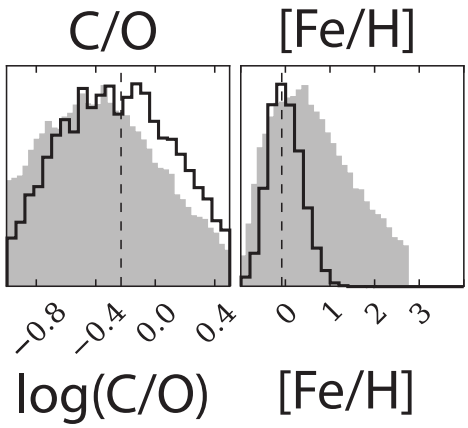

Figure 10. Comparison between the classic "free" retrieval approach used in this work and the "chemically consistent" approach for the $\lambda = 1-11$ μm emission spectrum of the warm sub-Neptune solar composition atmosphere. The gray solid histograms show the same values as in the top row of Fig. 8 ($1-11$ μm wavelengths). The black unfilled histograms are from the thermochemically-consistent retrieval. The log (C/O) histograms are in good agreement, both indicating poor constraint of C/O for this planetary atmosphere. However, the [Fe/H] metallicity histograms are substantially different due to the imposition of thermochemical consistency.

imately 215 K, 40 K, and 30 K respectively. Therefore the temperature inversion is detected at better than 4σ, 21σ, and 28σ respectively when using multiple retrieved T-P points in this pressure range. It is clear that the $\lambda > 2.5$ μm data constrain the hot Jupiter T-P profile much better than the $\lambda = 1-2.5$ μm data alone, and Fig. 11 shows that $\lambda = 1-11$ μm data constrain T-P profiles somewhat better than $\lambda = 1-5$ μm data for all 3 planets studied.

5.5. *HMMW Atmospheres and [Fe/H]*

The compositions of high mean molecular weight (including 100% H_2O) atmospheres will also be possible to constrain with JWST spectra. Figures 7 – 9 show that the transmission retrievals of the warm Neptune, warm sub-Neptune and cool super-Earth HMMW atmospheres have significantly different molecular mixing ratio distributions than the solar ones (with or without clouds; as expected from Table 3). Likewise, their [Fe/H] distributions are also significantly different, reflective of the high metallicity ([Fe/H] $\simeq 3$) required to produce HMMW atmospheres. These differences are readily apparent in the $\lambda = 1-2.5$ μm results alone in most cases, but they become more clear when longer wavelength data are included. Figures 7 – 8 and Table 5 clearly show that the emission retrievals constrain the warm Neptune and warm sub-Neptune clear HMMW atmospheres less well than transmission ones. These figures also show that the derived [Fe/H] values have uncertainties of ∼0.5 dex

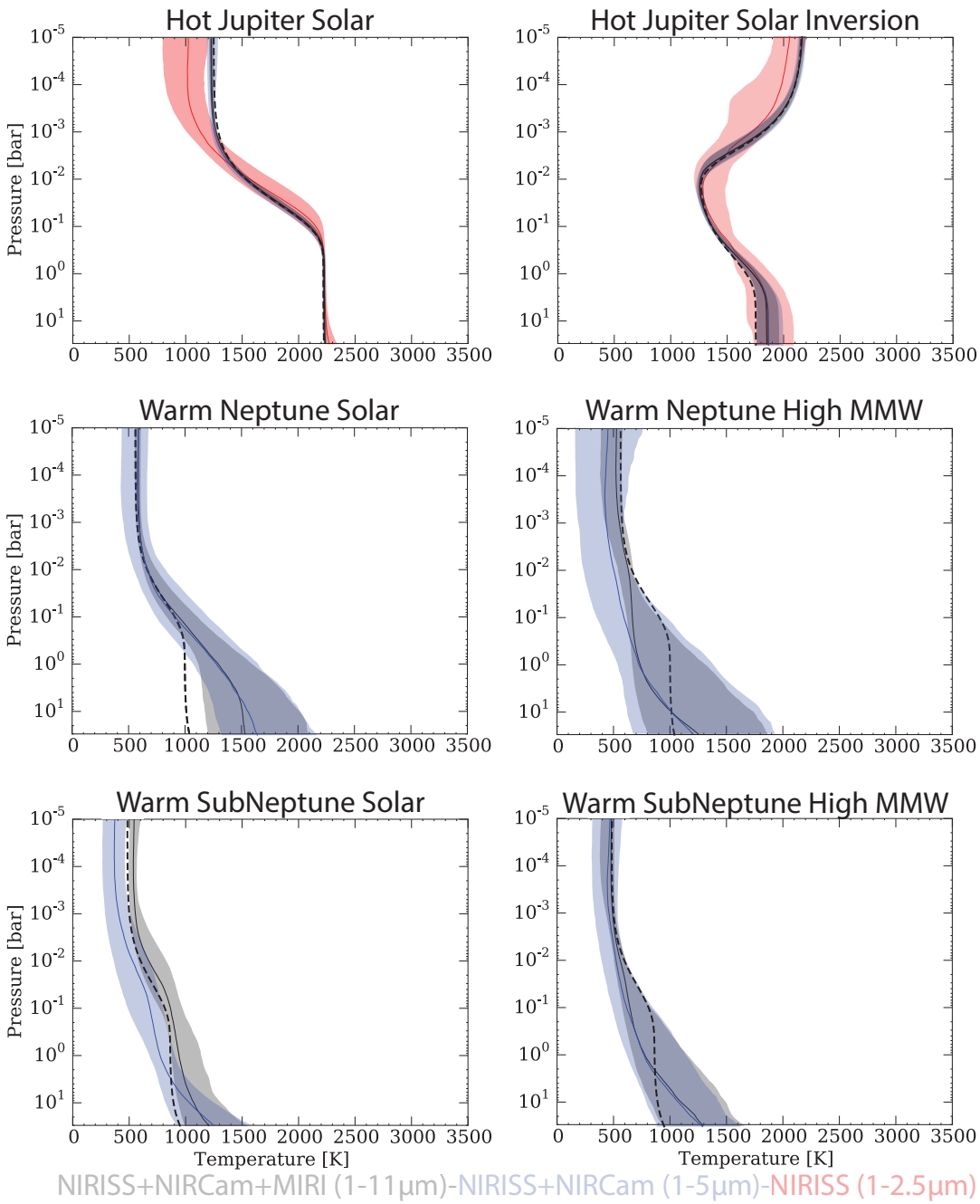

Figure 11. Temperature-Pressure (T-P) profiles retrieved from emission spectra. True values are shown as dashed lines. Solid lines are best fit retrieved values, and shaded regions denote 1σ uncertainties. Note that shadings are color coded by instrument mode and therefore the wavelengths of spectra used for retrievals. Sections of the temperature pressure profiles outside of well-constrained regions (see text and Fig. 12) are extrapolated from the temperature profile parameterization.

(factor of 3) or better for the clear (HMMW and solar composition) atmospheres of the hot and warm planets studied with $\lambda = 1 - 5+$ μm transmission spectra.

5.6. *Potential missing species and opacity uncertainties*

Real planets may have atmospheric species not included in the forward models or retrievals we have performed here. If this were the case, performing these retrievals on real JWST data would produce wavelength-dependent residual differences between observed and modeled spectra. Additional species could then be introduced into the model to minimize these residuals. Computing the Bayes factor between the models with simpler and more complex compositions would reveal whether adding the additional species is statistically justified. Uncertain molecular opacities may also skew the retrieved compositions for observed planets. However, this error is likely to be on the order of 10% but can be

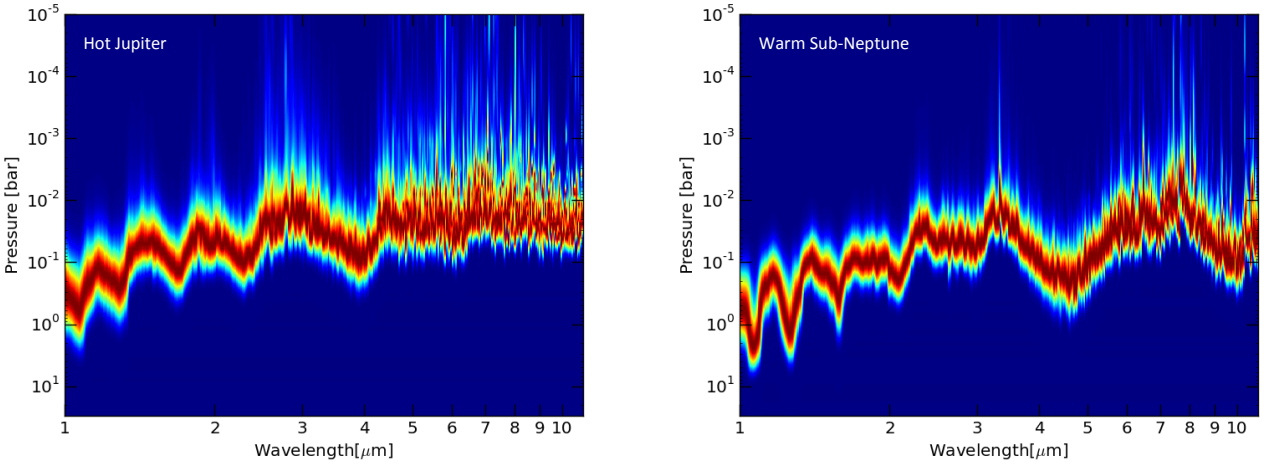

Figure 12. Normalized thermal emission contribution functions for the solar composition hot Jupiter (left) and warm sub-Neptune (right) planets. The figure shows the derivative of transmittance with altitude weighted by the planck function at that level. Dark red areas are where the emission predominantly originates whereas blue areas represent little or no emission. The pressure levels probed by the red areas contribute most to the retrieved composition and thermal structure information (e.g., see Line et al. 2013a, 2014a). The warm Neptune solar composition contribution function is very similar to the warm sub-Neptune one.

as high as a factor of a few in some cases (Grimm & Heng 2015, §3.4). This is mostly less than or equal to our best 68% mixing ratio confidence widths (see Table 5).

6. DISCUSSION

Here we discuss how applying these precision molecular abundance and temperature constraints may address several significant outstanding scientific issues. We focus on questions probing planet formation and disequilibrium chemistry and end with observational considerations that will impact data quality and the uncertainties of retrieved values.

6.1. *Carbon-to-Oxygen Ratios*

The C-to-O ratio (C/O) of a planetary atmosphere could be a tracer of its formation and migration history within a protoplanetary disk (Öberg et al. 2011). Determining the C/Os of a diverse set of exoplanets over a wide range of conditions is important for applying this theory to understand planet formation scenarios. There has yet to be unambiguous evidence for high C/O (C/O > 1) within the current ensemble of observed exoplanets (Konopacky et al. 2013; Barman et al. 2015; Madhusudhan et al. 2011; Line et al. 2014a; Stevenson et al. 2014; Kreidberg et al. 2015; Benneke 2015). Only upper limits (Kreidberg et al. 2015; Benneke 2015) have been derived from transmission spectra. Emission spectra retrievals have also provided upper limits for some planets or otherwise unconstrained, and a specific C/O value has only been determined for HD189733b which has broad near continuous wavelength coverage from ∼1 - 20 μm (Line et al. 2014a; Lee et al. 2012; Waldmann et al. 2015).

There are several ways of determining or diagnosing the C/O in exoplanet atmospheres. The most straightforward, direct approach, is to simply determine the abundance of all of the carbon and oxygen bearing species present in the spectra and compute it directly by summing the carbon atoms in all of the carbon species and dividing by the oxygen atoms in all the oxygen-bearing species. Certainly it is possible for some carbon or oxygen to be locked away in condensates or other species that may not necessarily present themselves spectroscopically resulting in a potential bias. In any case, this is the approach we take. Figures 6 – 9 show the C/O histograms derived from the retrieved molecular abundances. In some cases, when the abundances are not well constrained, a two peak distribution exists. This is simply due to the propagation of uniform-in-log priors through the ratio used to compute the C/O (see Line et al. 2013a, for an in depth discussion). Another approach is to retrieve the C/O directly as done by Kreidberg et al. (2015), Benneke (2015), and in §5.1 for a test case. However doing so requires the *assumption* of the chemical processes (e.g., thermochemical equilibrium, vertical mixing, photochemistry) via a chemical model that relates the elemental abundances to the molecular abundances (see §5.1).

We find that for all of the hot Jupiter transmission and emission scenarios observed with wavelengths longer than 2.5 μm (e.g., NIRISS+NIRCam and NIRISS+NIRCam+MIRI) the C/O can be constrained to better than 0.2 dex (factor of 1.6) and are largely unbiased by the two-peak problem. Wavelengths below 2.5 μm do not capture the strong CH_4, CO, or CO_2 vibrational bands that occur at longer wavelengths. The low abundance of CH_4 requires observation of the strong 3.3 and / or 7.7 μm band to provide a meaningful upper limit as CH_4 is not thermochemically dominant in hot atmospheres. While CO and CO_2 are dominant in hot atmospheres, they have a relatively narrow influence across wavelength. Furthermore, there is little improvement extending coverage beyond 5 μm as the strongest CO or CO_2 bands over the full $1 - 11$ μm wavelength range occurs at ∼4.5 μm (see Figure 1). Therefore, for hot Jupiters with comparable SNRs, observations over $\lambda = 1 - 5$ μm are more than sufficient to provide a meaningful constraint on their C/O.

The transmission spectra of warm Neptune and sub-Neptune low mean molecular weight (solar composition) clear atmospheres also unbiasedly constrain the C/O to

$\sim$0.2 dex or better in all three wavelength ranges. This is because the CH_4 is largely constrained to abundances that are greater than the CO or CO_2 abundances and thus the C/O ratio is mainly set by the methane-to-water ratio (CH_4/H_2O). Because of the large abundance of CH_4 in the cooler planets, it presents strong spectral features at wavelengths below 2.5 μm (see Figure 1). Even in the cloudy scenarios the log(C/O) constraints are only a factor of 1.2 worse.

Emission spectra constrain C/O less well in these small warm planets. $1-11$ μm emission spectra constrain C/O to $\sim$0.5 dex in the warm Neptune solar composition atmosphere, and $1-5$ μm emission spectra also provide some constraint (to only $\sim$1 dex). The $\lambda \geq 5$ μm emission spectra provide only loose constraints on C/O in the warm sub-Neptune clear solar atmosphere. Even complete $1-11$ μm emission spectra produce C/O distributions very similar to the priors for the high mean molecular weight atmospheres of these planets. These relatively cool planets have low flux and therefore low SNR near the $\lambda \leq 4$ μm CH_4 bands, so these results are not particularly surprising.

In general, the C/O constraints are poor for the cool super-Earth atmospheres. None of the transmission scenarios constrain C/O to significantly better than an order of magnitude.

Finally, Figure 13 shows how the retrieved H_2O mixing ratio uncertainties compare to the predicted thermochemical H_2O values for two different C/O cases (see Kreidberg et al. 2015). The uncertainties in H_2O mixing ratios are shown for the different planets' transmission cases (their positions are located for clarity and are not indicative of true temperatures or compositions). The H_2O mixing ratio depends on metallicity and contains no direct information on carbon abundance, so it cannot provide an unambiguous C/O constraint by itself. However it is instructive to show how one could use H_2O to rule out a high C/O scenario in some cases. For hot Jupiters, where the difference between solar and high C/O chemical models is largest, a measurement in a clear atmosphere could distinguish the difference between a solar and high C/O atmosphere by greater than 50σ for all 3 wavelength ranges. Using H_2O alone becomes difficult for planets with scale height temperatures below $T \sim$1000 K as the predicted thermochemical H_2O abundances converge for both solar value and high C/O. Other proxies such as the ratio of H_2O to CH_4 (under the assumption that oxidized carbon will be in low abundance; see Fig. 2 of Madhusudhan 2012) or a direct determination of the C/O (as above) will be required.

Regardless of the methodology used, it appears that JWST spectra will be very useful in determining the C-to-O ratios in a wide array of planetary atmospheres and will allow us to begin to address quantitatively the formation location relative to ice lines and any subsequent migration.

6.2. *The Mass-Metallicity Relationship*

Understanding planet formation requires determining and interpreting the mass-metallicity relationship for a varied sample of planets. Establishing this relationship over the exoplanet population provides insight into the core accretion formation mechanism (e.g., Ida & Lin 2005). There has been some progress on establishing

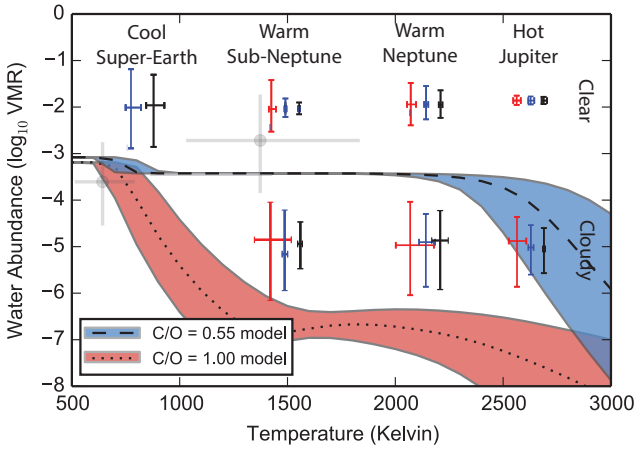

Figure 13. Application of precision H_2O and scale height temperature measurements from transmission spectra to distinguishing between high and low C/O scenarios (after Kreidberg et al. 2015). The broad red and blue curves are equilibrium chemistry models that show how the H_2O abundance changes as a function of temperature for high (red) and low (blue) C-to-O ratios for solar metallicity. The spread in the equilibrium chemistry models is due to different assumptions regarding the probed pressure levels (0.1 - 10 mbar). We show representative error bars derived from our temperature and H_2O retrieval results for the solar metallicity scenarios observed in transmission (Table 5). The red error bars represent the NIRISS only, blue are for NIRISS+NIRCam, and black are for NIRISS+NIRCam+MIRI. The top set error symbols show the constraints in the clear atmospheres and the bottom show cloudy ones. *These positions are located for clarity and are not indicative of actual retrieved temperatures or compositions!* The light gray points and error bars are constraints from HST WFC3 transmission measurements of WASP-12b (Kreidberg et al. 2015) (hotter) and WASP-43b KBD14b (cooler).

the role that planetary mass and parent star metallicity have in determining the *bulk* metallicity of transiting gas giants (Miller & Fortney 2011) through the use of planetary evolution models. A corresponding constraint on planetary atmospheric metallicity, from spectroscopy, would help us to understand if most of these metals are found in a core, or are mixed within the H/He-dominated envelope.

Using population synthesis models (Mordasini et al. 2012), Fortney et al. (2013) suggests that as the mass of a planet decreases, the atmospheric metallicity increases. Lower mass planets are unable to accrete substantial envelopes within the core-accretion theory and thus are more susceptible to pollution by in falling planetesimals. We do indeed find tantalizing evidence for such a trend within our own solar system as seen in Figure 14. However, in our own solar system we are limited to using CH_4 as the proxy for metallicity as water is largely sequestered in deep clouds. Exoplanet atmospheres, due to their high temperatures, permit us to access a wide array of molecules allowing for more precise constraints on the envelope metallicity. Kreidberg et al. (2014b) provided additional leverage on this relationship via a relatively good constraint on the water abundance in a 2 M_J hot Jupiter. Under the assumption of solar C/O, the retrieved water abundance was used as a proxy for metallicity. This proxy-metallicity was found to be consistent with the observed solar system trend. Furthermore, constraints of Neptune mass objects (GJ 436b by Stevenson et al. 2010 and HAT-P-11b by Fraine et al. 2014 are also

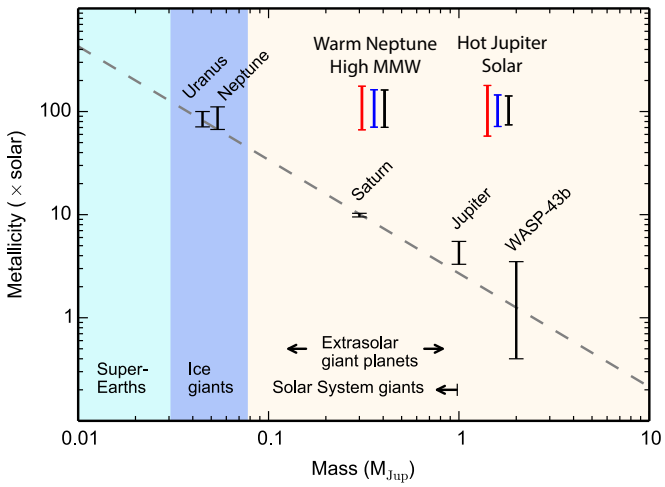

Figure 14. Atmospheric mass-metallicity relationship (after Kreidberg et al. (2014b)). Solar System planets and a measured exoplanet are shown as the black points with error bars. Representative transmission spectra metallicity constraints for a clear solar composition hot Jupiter and a clear high mean molecular weight warm Neptune are shown near the top (*not at their actual mass/metallicity values*). Three 68% confidence constraints are shown for each: black for NIRISS+NIRCam+MIRI, blue for NIRISS+NIRCam, and red for NIRISS only.

suggestive of this trend.

Recently, Benneke (2015) demonstrated that the water abundance alone cannot constrain the atmospheric metallicity because of the degeneracy of metallicity with the carbon-to-oxygen ratio. The broad wavelength coverage and high SNR of JWST data enable us to constrain not only the water abundance, but carbon species as well. This in essence, breaks the C/O-metallicity degeneracy. We directly compute the metallicity ([Fe/H]) from the retrieved molecular mixing ratios, and the metallicity histograms are shown in Figures 6 – 9 (see §5). Figure 14 compares a typical metallicity constraint for a solar composition hot Jupiter and a high mean molecular weight warm Neptune. Observing just 5 planets logarithmically spaced between a few Jupiter masses and a Neptune mass with such constraints (0.4 dex) would allow us to determine the mass-metallicity slope (in log space) with a 1σ uncertainty of 0.13.

6.3. *Disequilibrium Chemistry*

Disequilibrium processes are likely to play a role in sculpting the molecular abundances in exoplanet atmospheres (Liang et al. 2003; Zahnle et al. 2009; Line et al. 2010; Moses et al. 2011; Line et al. 2011; Venot et al. 2012; Agúndez et al. 2014; Hu et al. 2013). These processes come in a variety of flavors including, but not limited to vertical and horizontal mixing (Prinn & Barshay 1977; Cooper & Showman 2006), photochemistry (Yung & Demore 1999), ion chemistry (Lavvas et al. 2008), and biology (e.g., Holland 1994). The predicted dominant disequilibrium process in jovian-type planets is due to vertical mixing and thus we focus on the ability of JWST to infer disequilibrium due to vertical mixing. Vertical mixing tends to set (or quench) the upper atmospheric abundance of certain molecules to a particular deep atmospheric value which can result in an orders-of-magnitude enhancement (or depletion) relative to the expected equilibrium abundance at a higher altitude in the atmosphere. Line & Yung (2013) devised a scheme to determine the degree to which an atmosphere is out of equilibrium given the retrieved abundances of H_2O, CH_4, CO, and H_2. If these values form a ratio, α,

$$\alpha(f_i, P) = \frac{f_{CH_4} f_{H_2O}}{f_{CO} f_{H_2}^3 P^2} = K_{eq}(T) \quad (8)$$

where f_i are the molecular mixing ratios of species i, P is the pressure in bars, and T, temperature in K, that is equivalent to the thermochemical equilibrium constant $K_{eq}(T)$, than those species are considered to be in chemical equilibrium and thus disequilibrium mechanisms are weak or non-existent.

Figure 15 summarizes the constraints on α as provided by the different wavelength regions for emission sectra. We also note, as in Line & Yung (2013), that there could be up to a factor of ∼100 more uncertainty due to the spread in the probed pressure levels. Furthermore, in some cases only an upper limit on one of the three retrieved gases can be obtained. In these cases α would also only have an upper or lower limit. We find that the hot Jupiter scenarios will have the best constraint on α. Unfortunately hot Jupiters are generally predicted to be in equilibrium (Line & Yung 2013), so the small error bar is not very useful for identifying disequilibrium in those planets. The objects cooler than ∼1000 K will likely show signs of disequilibrium due to the dredging up of CO (and also N_2 in the NH_3–N_2 chemical system). This will result in an α that falls below the equilibrium line. The maximum expected deviation due to strong vertical mixing is only $\sim 2\sigma$ larger than the smallest warm Neptune error bar, making the definitive detection of disequilibrium due to vertical mixing difficult. Perhaps the best way of approaching this problem is to determine α over a wide range of planetary effective temperatures to identify where deviations from equilibrium begin to occur. This transition is likely to occur between 1000–1200 K (e.g., Moses et al. 2011). This temperature region is also a good place to observe because the CH_4 and CO abundances begin to thermochemically trade places. Their near equal abundances and the higher temperatures (relative to the warm Neptunes) will likely allow bounded constraints on both the CO and CH_4 abundances providing an actual bounded constraint on α.

We have broadly explored the detectability of disequilibrium due to vertical mixing. Certainly, photochemistry can produce species not included in this investigation (e.g., C_mH_n, HCN), especially in cooler planets in which CH_4 is readily available for photolysis (Line et al. 2011; Venot et al. 2014; Moses et al. 2013; Hu & Seager 2014; Miller-Ricci Kempton et al. 2012). Shabram et al. (2011) determined that some of these photoproducts are potentially detectable in JWST observations of planets similar to the warm Neptune (GJ 436b) we have considered here.

6.4. *Additional Observational Considerations*

The precision of the retrieved parameters are limited by the particular star-planet systems chosen as well as the planets themselves. For example, the H_2O mixing ratio uncertainty using all wavelengths is considerably better for the warm sub-Neptune (0.25 dex) versus the warm Neptune (0.59 dex) clear solar atmosphere in

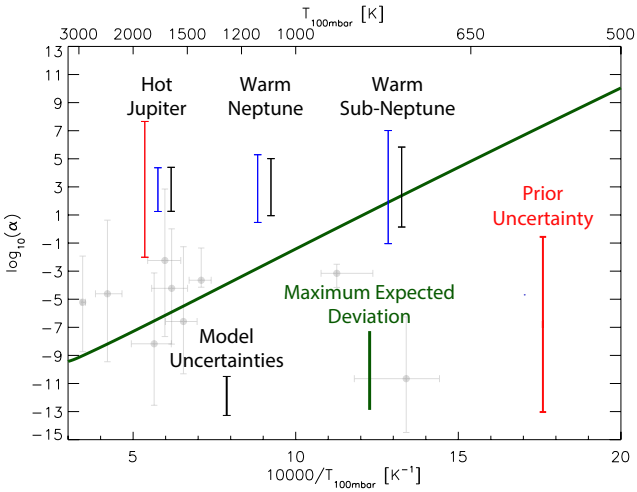

Figure 15. Diagnosing disequilbirum chemistry with JWST (adapted from Line & Yung 2013). The green line is the equilibrium constant as a function of temperature. Given the equilibrium molecular abundances of H_2O, CH_4, CO and H_2 at a given temperature and pressure, the quantity α (see Eq. 8) will fall on this line. If there are strong disequilibrium processes, α will deviate from the green line. α computed from the retrieved abundances for H_2O, CH_4, CO and H_2 for a variety of planets observed with HST and Spitzer are shown in light gray (Line & Yung 2013; Line et al. 2014a). We show representative error bars for α derived from the retrieved mixing ratios of emission spectra for the hot Jupiter, warm Neptune, and warm Sub-Neptune solar composition emission scenarios for NIRISS only (red), NIRISS+NIRCam (blue), and NIRISS+NIRCam+MIRI (black). *Their positions in the plot are arbitrary.* Model uncertainty due to the uncertainty in the pressure levels probed (e.g., the width of the thermal emission contribution function across wavelength) is shown as the black error bar. The maximum expected deviation due to vertical mixing is shown as the green error bar. Finally, the prior uncertainty is shown as the red curve.

transmission. These two planets have similar equilibrium temperatures and scale heights (see Table 2), so this difference is likely due to the higher SNR of the warm sub-Neptune simulations caused by the relatively high brightness and small size of the adopted host star, GJ 1214. Each star+planet system should be evaluated to determine whether emission or transmission observations are more favorable for detecting spectral features and constraining parameters of interest. The planetary system parameters given in Table 2 should be useful for scaling these results to other systems.

We do not know how well co-adding observations of multiple transits or secondary eclipses will improve our results at this time. The simulated single transit and single eclipse observations of our selected systems typically have total noise values only $10-50\%$ larger than our adopted noise floors (§4), so systematic noise assumptions have already significantly influenced the precision of our simulated data and retrieved information. Given this, co-adding more data would not substantially improve the results for these very observationally favored systems with bright host stars. We believe that our systematic noise assumptions are reasonable, but we will not know their exact values in different conditions (e.g., co-adding multiple spectra vs. binning to lower resolution) until after JWST becomes operational.

Other instrumental and astrophysical noise sources may also impact JWST data. Barstow et al. (2015) considered the impact of systematic wavelength-invariant offsets between the spectra acquired in different JWST instrument modes. They found that the impact on retrieved parameters was minimal if even small regions of overlap between the modes were used to correct such errors to below the noise of their simulations. This is also likely to apply in our study if residual offsets between the different spectral regions are (corrected to) less than their respective adopted systematic noise floors. We note that the different instrument modes have more spectral overlap than the regions we selected in Table 4.

Barstow et al. (2015) also note that star spots can impact transmission (but not emission) spectra considerably (see also Pont et al. 2013) and assess their impact on retrievals of planet parameters for both solar- and M-type (T_{eff} = 3000 K) host stars. They find that the quality of retrieved information is not seriously degraded for a hot Jupiter with a Sun-like star that has a relatively high spot fraction (3% of its area). However, Barstow et al. (2015) find that the retrieved H_2O mixing ratio can be up to an order of magnitude too high for the transmission spectrum of a hot Neptune planet with an M-type host star with a spot coverage of 10% if the planet does not occult any spots during transit. This error is considerably larger than the H_2O mixing ratio uncertainty we expect for the warm Neptune with a clear solar composition atmosphere and full $1-11$ μm wavelength coverage (Table 5), and we share the concern with Barstow et al. (2015) that stellar activity could be the limiting factor for accurate retrievals of JWST observations of active stars. Simultaneous photometric observations at relatively short wavelengths (e.g., see Fraine et al. 2014) could be used to correct this effect, and this may be possible with NIRCam $\lambda \leq 2.4$ μm imaging during the NIRCam $\lambda = 2.5-5.0$ μm grism spectral observations.

7. SUMMARY AND CONCLUSIONS

We have generated forward models of transmission and emission spectra of generic hot Jupiter, warm Neptune, warm sub-Neptune, and cool super-Earth planets using the parameters of well-known systems. We then performed simulations of slitless JWST observations using the instrument modes NIRISS SOSS over $1-2.5$ μm, the NIRCam grisms over $2.5-5.0$ μm (2 exposures required), and the MIRI LRS over $5.0-11$ μm. The NIRSpec instrument may be used instead of NIRCam, but it also requires 2 exposures over $2.5-5.0$ μm for bright stars, and we understand its likely systematic noise less well than NIRCam at this time. We performed retrievals on single simulated transits and secondary eclipses to assess what information and constraints JWST data are likely to provide on these planet archetypes and other exoplanet atmospheres. We arrive at following major conclusions:

1. JWST will likely obtain high quality transmission and emission spectra of a variety of exoplanet atmospheres over a wavelength range of at least $1-11$ μm. Obtaining spectra over this entire range will typically require observations of 4 separate transit or secondary eclipse events using 4 instrument modes for planets with bright host stars. We do not know at this time exactly how JWST data will be impacted by systematic noise, but we have assumed noise floors consistent with the best performance of

HST or Spitzer as appropriate for each wavelength range.

2. The volume mixing ratios of dominant molecular species, C/O, and [Fe/H] of clear solar composition planetary atmospheres can be diagnosed very well with transmission spectra, often with only $1-2.5$ μm wavelength NIRISS data. However, longer wavelength data are needed for good constraints in some cases. Strong temperature inversions should be detectable in the T-P profile of the clear solar composition hot Jupiter planet with emission spectra covering $\lambda = 1-2.5$ μm. The T-P profiles of the hot Jupiter, warm Neptune, and warm sub-Neptune are all constrained reasonably well with $1-5$ μm emission spectra. JWST transmission spectra will be useful for discriminating between cloudy and HMMW atmospheres of small planets in observationally favorable systems.

3. JWST spectra have the potential to constrain the molecular mixing ratios, C/O, [Fe/H], and T-P profiles of planets with cloudy atmospheres. Mixing ratios of the cloudy warm sub-Neptune is constrained to ~ 1 dex with transmission spectra covering $\lambda = 1-11$ μm. However, $\lambda = 1-11$ μm emission spectra provide significantly better constraints than the transmission spectra on the mixing ratios of most molecules for cloudy hot Jupiter and warm Neptune atmospheres assuming that emission spectra are not impacted by clouds. Each star+planet system should be evaluated to determine whether emission or transmission observations are more favorable for detecting spectral features and constraining parameters of interest. Emission spectra can be more useful than transmission in cases of sufficiently high F_p accompanied by high F_p/F_*. Acquiring both transmission and emission spectra will probe exoplanet atmospheres over the broadest possible pressure ranges and constrain compositions and chemistries better than either transmission or emission alone.

4. The complete $\lambda = 1-11$ μm cool super-Earth emission spectrum had insufficient signal-to-noise for retrievals. There simply is not enough flux contrast F_p/F_* for useful emission spectra from this system when a single secondary eclipse is observed at each wavelength. Photometric filter observations may be more useful for constraining the planet's properties. Small ($R \lesssim 2R_\oplus$), cool ($T <$700 K) planets will need host stars with $K \lesssim 8.5$ mag and / or spectral types later than M0 V for useful emission spectra of single secondary eclipses.

5. The molecular mixing ratios retrieved from $\lambda = 1-5+$ μm JWST transmission spectra will provide derived [Fe/H] values with an uncertainty of 0.5 dex (factor of 3) or better for the clear atmospheres of the hot and warm planets studied. This is adequate for evaluating systematic differences in metallicity with planet mass and determining whether this function is substantively similar to or different from our Solar System.

6. Carbon-to-oxygen ratios derived from the retrieved molecular mixing ratios are constrained to better than 0.2 dex (factor of 1.6) for the hot Jupiter system when using $\lambda \geq 5$ μm transmission or emission spectra. H_2O mixing ratio values and retrieved atmospheric temperatures can also be used to distinguish between high (1.0) and solar (0.55) C/O values for hot planets (and with only $\lambda \leq 2.5$ μm transmission data in many cases), sufficient for assessing whether they formed interior to or exterior of the H_2O ice lines in their protoplanetary disks. Transmission spectra constrain C/O better than emission spectra for the warm Neptune and sub-Neptune systems. $\lambda \geq 5$ μm spectra provide the best constraints for these warm planets, but $\lambda = 1-2.5$ μm data give good results for clear solar atmospheres.

7. The uncertainties in molecular mixing ratios retrieved from JWST emission spectra (even $\lambda \geq 5$ μm) for single observations are too large to obtain a definitive detection of vertical mixing via the method of Line et al. (2013b). However, observing many planets that span a range of effective temperatures should permit us to identify at which temperatures the molecular abundances deviate from equilibrium. The ensemble of retrieved mixing ratio values and uncertainties of the planets studied here can be used to assess how well each species can be detected in observations of real planets that may have different compositions (e.g., the sensitivity to CO or CO_2 in cool planets). The detection limits presented here should be scaled to the SNR of any real data, and similar wavelength ranges should be used in such comparisons.

8. We not know at this time how well SNR and retrieval uncertainties will improve with the binning or co-addition of data beyond the single transit or eclipse observations simulated here. We hope and expect that this work will be useful for planning early JWST observations, but actual on-orbit performance must be measured to make better predictions.

We are grateful to L. Albert, J. Barstow, J. Bean, S. Birkmann, J. Bouwman, R. Doyon, P. Ferruit, Th. Henning, L. Kreidberg, P.-O. Lagage, N. Lewis, M. Marley, and the JWST NIRCam and MIRI instrument teams for helpful science discussions, feedback, and information on instrument performance. We also thank the referee I. Crossfield whose numerous insightful recommendations and comments allowed us to substantially improve the paper. This research has made use of the Exoplanet Orbit Database and the Exoplanet Data Explorer at exoplanets.org. The simulations for this research were carried out on the UCSC supercomputer Hyades, which is supported by National Science Foundation (award number AST-1229745) and University of California, Santa Cruz. TPG acknowledges support from the NASA JWST Project and Program for this work via WBSs 411672.04.01.02 and 411672.05.05.02.02. MRL acknowledges support provided by NASA through Hubble

Fellowship grant #51362 awarded by the Space Telescope Science Institute, which is operated by the Association of Universities for Research in Astronomy, Inc., for NASA, under the contract NAS 5-26555. JJF acknowledges the support of NSF grant AST-1312545.

Facilities: JWST.

REFERENCES

Agúndez, M., Parmentier, V., Venot, O., Hersant, F., & Selsis, F. 2014, A&A, 564, A73
Almenara, J. M., Astudillo-Defru, N., Bonfils, X., et al. 2015, A&A, 581, L7
Barman, T. S., Konopacky, Q. M., Macintosh, B., & Marois, C. 2015, ApJ, 804, 61
Barstow, J. K., Aigrain, S., Irwin, P. G. J., Kendrew, S., & Fletcher, L. N. 2015, MNRAS, 451, 1306
Barstow, J. K., Aigrain, S., Irwin, P. G. J., et al. 2013, MNRAS, 430, 1188 (2013a)
Barstow, J. K., Aigrain, S., Irwin, P. G. J., Fletcher, L. N., & Lee, J.-M. 2013, MNRAS, 434, 2616 (2013b)
Batalha, N., Kalirai, J., Lunine, J., Clampin, M., & Lindler, D. 2015, arXiv:1507.02655
Beichman, C., Benneke, B., Knutson, H., et al. 2014, PASP, 126, 1134
Benneke, B. 2015, arXiv:1504.07655
Benneke, B., & Seager, S. 2012, ApJ, 753, 100
Benneke, B., & Seager, S. 2013, ApJ, 778, 153
Brown, T. M. 2001, ApJ, 553, 1006
Burrows, A. S. 2014, Proceedings of the National Academy of Science, 111, 12601
Burrows, A., & Orton, G. 2010, Exoplanets, 419
Christiansen, J. L., Ballard, S., Charbonneau, D., et al. 2010, ApJ, 710, 97
Cooper, C. S., & Showman, A. P. 2006, ApJ, 649, 1048
Cowan, N. B., Greene, T., Angerhausen, D., et al. 2015, PASP, 127, 311
Croll, B., Albert, L., Jayawardhana, R., et al. 2011, ApJ, 736, 78
Crossfield, I. J. M. 2015, PASP, 127, 941
Crossfield, I. J. M., Petigura, E., Schlieder, J., et al. 2015, ApJ, 804, 10
Crouzet, N., McCullough, P. R., Burke, C., & Long, D. 2012, ApJ, 761, 7
Deming, D., Seager, S., Winn, J., et al. 2009, PASP, 121, 952
Deming, D., Wilkins, A., McCullough, P., et al. 2013, ApJ, 774, 95
Diamond-Lowe, H., Stevenson, K. B., Bean, J. L., Line, M. R., & Fortney, J. J. 2014, ApJ, 796, 66
Doyon, R., Hutchings, J. B., Beaulieu, M., et al. 2012, Proc. SPIE, 8442
Ferruit, P., Birkmann, S., Böker, T., et al. 2014, Proc. SPIE, 9143, 91430A
Foreman-Mackey, D., Hogg, D. W., & Morton, T. D. 2014, ApJ, 795, 64
Fortney, J. J. 2005, MNRAS, 364, 649
Fortney, J. J., Ikoma, M., Nettelmann, N., Guillot, T., & Marley, M. S. 2011, ApJ, 729, 32
Fortney, J. J., Lodders, K., Marley, M. S., & Freedman, R. S. 2008, ApJ, 678, 1419
Fortney, J. J., Mordasini, C., Nettelmann, N., et al. 2013, ApJ, 775, 80
Fraine, J., Deming, D., Benneke, B., et al. 2014, Nature, 513, 526
Gibson, N. P., Pont, F., & Aigrain, S. 2011, MNRAS, 411, 2199
Gordon, S., & McBride, B. J. 1994, NASA Reference Publ. 1311, http://www.grc.nasa.gov/WWW/CEAWeb/RP-1311.pdf
Greene, T., Beichman, C., Eisenstein, D., et al. 2007, Proc. SPIE, 6693, 66930G
Grimm, S. L., & Heng, K. 2015, ApJ, 808, 182
Griffith, C. A. 2014, Philosophical Transactions of the Royal Society of London Series A, 372, 30086
Han, E., Wang, S. X., Wright, J. T., et al. 2014, PASP, 126, 827
Hauschildt, P. H., Allard, F., & Baron, E. 1999, ApJ, 512, 377
Haynes, K., Mandell, A. M., Madhusudhan, N., Deming, D., & Knutson, H. 2015, ApJ, 806, 146
Holland, H. D. 1994, in Early Life on Earth, ed. S. Bengtson, (New York, NY: Columbia University Press), 237
Heng, K., & Showman, A. P. 2015, Annual Review of Earth and Planetary Sciences, 43, 509
Hu, R., & Seager, S. 2014, ApJ, 784, 63
Hu, R., Seager, S., & Bains, W. 2013, ApJ, 769, 6
Ida, S., & Lin, D. N. C. 2005, ApJ, 626, 1045
Kataria, T., Showman, A. P., Fortney, J. J., et al. 2015, ApJ, 801, 86
Kendrew, S., Scheithauer, S., Bouchet, P., et al. 2015, PASP, 127, 623
Knutson, H. A., Charbonneau, D., Cowan, N. B., et al. 2009, ApJ, 703, 769
Knutson, H. A., Dragomir, D., Kreidberg, L., et al. 2014, ApJ, 794, 155
Knutson, H. A., Howard, A. W., & Isaacson, H. 2010, ApJ, 720, 1569
Konopacky, Q. M., Barman, T. S., Macintosh, B. A., & Marois, C. 2013, Science, 339, 1398
Kreidberg, L., Bean, J. L., Désert, J.-M., et al. 2014, Nature, 505, 69 (2014a)
Kreidberg, L., Bean, J. L., Désert, J.-M., et al. 2014, ApJ, 793, LL27 (2014b)
Kreidberg, L., Line, M. R., Bean, J. L., et al. 2015, arXiv:1504.05586
Lavvas, P. P., Coustenis, A., & Vardavas, I. M. 2008, Planet. Space Sci., 56, 27
Lecavelier Des Etangs, A., Vidal-Madjar, A., Désert, J.-M., & Sing, D. 2008, A&A, 485, 865
Lee, J.-M., Fletcher, L. N., & Irwin, P. G. J. 2012, MNRAS, 420, 170
Liang, M.-C., Parkinson, C. D., Lee, A. Y.-T., Yung, Y. L., & Seager, S. 2003, ApJ, 596, L247
Line, M. R., Fortney, J. J., Marley, M. S., & Sorahana, S. 2014, ApJ, 793, 33 (2014b)
Line, M. R., Knutson, H., Deming, D., Wilkins, A., & Desert, J.-M. 2013, ApJ, 778, 183 (2013b)
Line, M. R., Knutson, H., Wolf, A. S., & Yung, Y. L. 2014, ApJ, 783, 70 (2014a)
Line, M. R., Liang, M. C., & Yung, Y. L. 2010, ApJ, 717, 496
Line, M. R., Teske, J., Burningham, B., Fortney, J. J., & Marley, M. S. 2015, ApJ, 807, 183
Line, M. R., Vasisht, G., Chen, P., Angerhausen, D., & Yung, Y. L. 2011, ApJ, 738, 32
Line, M. R., Wolf, A. S., Zhang, X., et al. 2013, ApJ, 775, 137 (2013a)
Line, M. R., & Yung, Y. L. 2013, ApJ, 779, 3
Line, M. R., Zhang, X., Vasisht, G., et al. 2012, ApJ, 749, 93
Madhusudhan, N. 2012, ApJ, 758, 36
Madhusudhan, N., Harrington, J., Stevenson, K. B., et al. 2011, Nature, 469, 64
Madhusudhan, N., Knutson, H., Fortney, J. J., & Barman, T. 2014, Protostars and Planets VI, 739
Madhusudhan, N., & Seager, S. 2009, ApJ, 707, 24
McCullough, P. R., Crouzet, N., Deming, D., & Madhusudhan, N. 2014, ApJ, 791, 55
Miller, N., & Fortney, J. J. 2011, ApJ, 736, L29
Miller-Ricci Kempton, E., Zahnle, K., & Fortney, J. J. 2012, ApJ, 745, 3
Mordasini, C., Alibert, Y., Klahr, H., & Henning, T. 2012, A&A, 547, A111
Moses, J. I., Line, M. R., Visscher, C., et al. 2013, ApJ, 777, 34
Moses, J. I., Visscher, C., Fortney, J. J., et al. 2011, ApJ, 737, 15
Öberg, K. I., Murray-Clay, R., & Bergin, E. A. 2011, ApJ, 743, L16
Pont, F., Sing, D. K., Gibson, N. P., et al. 2013, MNRAS, 432, 2917
Prinn, R. G., & Barshay, S. S. 1977, Science, 198, 1031
Schwieterman, E. W., Robinson, T. D., Meadows, V. S., Misra, A., & Domagal-Goldman, S. 2015, ApJ, 810, 57
Seager, S., & Deming, D. 2010, ARA&A, 48, 631
Schwarz, H., Brogi, M., de Kok, R., Birkby, J., & Snellen, I. 2015, A&A, 576, A111
Shabram, M., Fortney, J. J., Greene, T. P., & Freedman, R. S. 2011, ApJ, 727, 65

Stevenson, K. B., Bean, J. L., Madhusudhan, N., & Harrington, J. 2014, ApJ, 791, 36
Stevenson, K. B., Harrington, J., Nymeyer, S., et al. 2010, Nature, 464, 1161
Swain, M. R., Line, M. R., & Deroo, P. 2014, ApJ, 784, 133
Swain, M. R., Vasisht, G., Tinetti, G., et al. 2009, ApJ, 690, L114
Venot, O., Agúndez, M., Selsis, F., Tessenyi, M., & Iro, N. 2014, A&A, 562, A51
Venot, O., Hébrard, E., Agúndez, M., et al. 2012, A&A, 546, A43
Visscher, C., & Moses, J. I. 2011, ApJ, 738, 72
Waldmann, I. P., Tinetti, G., Rocchetto, M., et al. 2015, ApJ, 802, 107
Yung, Y. L., & Demore, W. B. 1999, Photochemistry of planetary atmospheres / Yuk L. Yung, William B. DeMore. New York : Oxford University Press, 1999. QB603.A85 Y86 1999
Zahnle, K., Marley, M. S., Freedman, R. S., Lodders, K., & Fortney, J. J. 2009, ApJ, 701, L20

Table 5
Retrieved Parameter Uncertainties or Limits[a]

Planet	λ (μm)	Geom	T(K)	xRp	log(P_c) (bar)	logH_2O	logCH_4	logCO	logCO_2	logNH3	logN2
Hot Jupiter											
Clear Solar	1 – 11	Trans	25	0.002	>-0.82	0.16	<-7.1	0.32	0.23	<-7.1	<-2.7
	1 – 5.0	Trans	28	0.002	>-0.77	0.17	<-7.1	0.34	0.25	<-6.5	<-2.7
	1 – 2.5	Trans	35	0.002	>-0.82	0.20	<-6.0	1.8	<-5.1	<-6.0	<-2.5
Cloud Solar	1 – 11	Trans	18	0.01	1.1	1.1	<-5.6	1.3	2.9[b]	<-5.5	<-2.4
	1 – 5.0	Trans	33	0.011	1.3	1.5	<-5.4	1.6	3.3[b]	<-4.6	<-1.8
	1 – 2.5	Trans	180	0.021	1.6	1.5	<-3.3	<-1.3	<-2.6	<-3.6	<-0.80
Solar	1 – 11	Emis				0.17	<-6.9	0.26	0.17	<-6.4	···
	1 – 5.0	Emis	···	···	···	0.22	<-6.9	0.36	0.23	<-5.9	···
	1 – 2.5	Emis	···	···	···	0.63	<-4.6	<-1.1	<-4.6	<-5.1	···
Solar	1 – 11	Emis	···	···	···	0.32	<-6.1	0.38	0.41	<-5.5	···
Inversion	1 – 5.0	Emis	···	···	···	0.36	<-5.8	0.44	0.53	<-5.2	···
	1 – 2.5	Emis	···	···	···	3.6	<-2.5	<-2.5	<-2.5	<-5.0	···
Warm Neptune											
Clear Solar	1 – 11	Trans	17	0.008	>-1.3	0.59	0.51	<-3.5	<-7.1	0.53	<-2.5
	1 – 5.0	Trans	19	0.010	>-1.4	0.71	0.61	<-3.3	<-7.1	0.63	<-2.4
	1 – 2.5	Trans	42	0.014	>-1.7	0.91	0.87	<-2.3	<-3.7	0.85	<-2.3
Cloud Solar	1 – 11	Trans	76	0.025	1.6	1.7	1.7	<-3.1	<-5.0	1.7	<-1.2
	1 – 5.0	Trans	74	0.020	1.5	1.6	1.5	<-2.9	<-4.9	3.6[b]	<-1.7
	1 – 2.5	Trans	180	0.029	1.9	2.0	1.9	<-0.9	<-2.4	<-1.8	<-0.50
High MMW	1 – 11	Trans	170	0.005	>-3.2	3.9[b]	1.6	<-0.10	1.6	<-2.5	<-0.20
	1 – 5.0	Trans	240	0.004	>-2.8	3.7[b]	1.8	<-0.20	1.8	<-2.7	<-0.20
	1 – 2.5	Trans	300	0.005	>-3.4	<-0.06	>-4.0	< -0.20	2.7	<-1.9	<-0.20
Solar	1 – 11	Emis	···	···	···	1.26	0.79	<-3.6	<-6.1	1.2	···
	1 – 5.0	Emis	···	···	···	2.4	1.5	<-2.4	<-5.7	4.7[b]	···
High MMW	1 – 11	Emis	···	···	···	<-1.6	2.1	<-1.2	>-6.2	<4.1	···
	1 – 5.0	Emis	···	···	···	–	4.3	<-1.8	–	<-0.7	
Warm Sub-Neptune											
Clear Solar	1 – 11	Trans	8.1	0.006	>-0.70	0.25	0.19	<-6.4	<-8.0	0.21	<-2.0
	1 – 5.0	Trans	9.8	0.009	> -0.8	0.40	0.30	<-6.1	<-7.9	0.31	<-2.5
	1 – 2.5	Trans	33	0.029	>-1.6	1.1	1.0	<-2.4	<-3.7	1.0	<-2.1
Cloud Solar	1 – 11	Trans	22	0.024	0.92	1.0	0.96	<-4.0	<-5.7	1.0	<-2.4
	1 – 5.0	Trans	25	0.044	1.6	1.7	1.6	<-5.4	<-5.9	1.6	<-2.2
	1 – 2.5	Trans	170	0.076	1.9	2.1	2.1	<-1.2	<-6.4	2.4	<-0.80
High MMW	1 – 11	Trans	100	0.004	>-3.3	1.0	0.65	<-0.4	0.84	<-2.4	<-0.10
	1 – 5.0	Trans	130	0.005	>-3.2	1.4	1.1	<-0.10	1.4	<-2.6	<-0.10
	1 – 2.5	Trans	200	0.007	>-3.4	>-5.0	1.2	<-0.20	<-0.50	<-1.8	<-0.10
Solar	1 – 11	Emis	···	···	···	2.2	1.5	<-1.4	<-4.7	2.2	···
	1 – 5.0	Emis	···	···	···	6.1[b]	2.5	<-1.7	<-4.6	<-0.50	···
High MMW	1 – 11	Emis	···	···	···	4.3[b]	2.3	<-0.50	3.2[b]	<-0.80	···
	1 – 5.0	Emis	···	···	···	<-0.10	–	< -2.1	5.0[b]	–	···
Cool Super-Earth											
Clear Solar	1 – 11	Trans	72	0.030	>-2.4	1.8	1.3	<-2.1	<-3.4	1.3	<-1.1
	1 – 5.0	Trans	85	0.028	>-2.5	1.9	1.3	<-2.1	<-3.3	1.3	<-1.1
	1 – 2.5	Trans	120	0.035	>-2.8	< −0.7	1.4	<-1.4	<-1.9	1.4	<-0.20
Cloud Solar	1 – 11	Trans	570	0.25	2.8	<-0.10	>-7.5	<-0.11	<-0.44	–	–
	1 – 5.0	Trans	700	0.200	>1.5	<-0.10	>-7.5	<-0.28	<-0.27	–	–
	1 – 2.5	Trans	<3000	0.33	>1.5	–	–	–	–	–	–
Clear H_2O	1 – 11	Trans	670	0.043	>-5.9	>-5.0	<-1.8	–	<-0.10	<-0.14	–
	1 – 5.0	Trans	720	0.044	>-5.9	>-7.0	<-1.4	–	<-0.10	<-0.50	–
	1 – 2.5	Trans	970	0.075	>-5.9	>-7.0	<-0.85	–	<-0.10	<-0.36	–

Note. — 68% confidence widths are given when parameters are well determined, otherwise 3-σ upper (<) or lower (>) value limits are listed. No constraint (the probability spans the prior range) is denoted by "–" non-retrieved values are denoted by " ··· ". To aid interpretation, an uncertainty of 0.3 corresponds to a constraint within a factor of 2, 0.7 within a factor of 5, and 1 within a factor of 10 for the log value parameters. All values are uncertain to ∼10% due to statistical jitter in MCMC retrievals and in the random noise instance applied to the simulated data.

[a] Retrieved parameters for transmission (Trans) and emission (Emis) spectra are described in §3

[b] 68% confidence width, but lower mixing ratio values are unconstrained at 2-σ